# ARTICLE

# Innate immune memory in the brain shapes neurological disease hallmarks

Ann-Christin Wendeln[1,2,3,12], Karoline Degenhardt[1,2,3,12], Lalit Kaurani[4,5], Michael Gertig[4,5], Thomas Ulas[6], Gaurav Jain[5,7], Jessica Wagner[1,2,3], Lisa M. Häsler[1,2], Katleen Wild[1,2], Angelos Skodras[1,2], Thomas Blank[8], Ori Staszewski[8], Moumita Datta[8], Tonatiuh Pena Centeno[5,7], Vincenzo Capece[5,7], Md. Rezaul Islam[5], Cemil Kerimoglu[5], Matthias Staufenbiel[1,2], Joachim L. Schultze[6,9], Marc Beyer[10], Marco Prinz[8,11], Mathias Jucker[1,2], André Fischer[4,5] & Jonas J. Neher[1,2]*

**Innate immune memory is a vital mechanism of myeloid cell plasticity that occurs in response to environmental stimuli and alters subsequent immune responses. Two types of immunological imprinting can be distinguished—training and tolerance. These are epigenetically mediated and enhance or suppress subsequent inflammation, respectively. Whether immune memory occurs in tissue-resident macrophages in vivo and how it may affect pathology remains largely unknown. Here we demonstrate that peripherally applied inflammatory stimuli induce acute immune training and tolerance in the brain and lead to differential epigenetic reprogramming of brain-resident macrophages (microglia) that persists for at least six months. Strikingly, in a mouse model of Alzheimer's pathology, immune training exacerbates cerebral β-amyloidosis and immune tolerance alleviates it; similarly, peripheral immune stimulation modifies pathological features after stroke. Our results identify immune memory in the brain as an important modifier of neuropathology.**

Contrary to the long-held assumption that immunological memory exists only in cells of the adaptive immune system, recent evidence has indicated that myeloid cells also display memory effects[1,2]. For example, certain immune stimuli train blood monocytes to generate enhanced immune responses to subsequent immune insults[3,4]. By contrast, other stimuli induce immune tolerance—suppression of inflammatory responses to subsequent stimuli[3,5]. Innate immune memory lasts for several days in vitro and for up to three months in circulating monocytes in vivo and is mediated by epigenetic reprogramming in cultured cells, with chromatin changes also apparent in vivo[3,6,7]. However, it is unclear whether immune memory occurs in long-lived tissue-resident macrophages and whether it alters tissue-specific pathology.

Microglia (brain-resident macrophages) are very long-lived cells[8,9]. This makes them particularly interesting for studying immune memory, as virtually permanent modification of their molecular profile appears possible. As microglia are also involved in many neurological diseases[10–12], we investigated whether immune memory occurs in microglia in vivo and how it affects neuropathology.

## Acute immune memory in the brain

It is well-established that inflammation in the periphery can prompt immune responses in the brain[13]. To evaluate whether immune memory can be induced in the brain by peripheral stimulation, we gave mice daily intraperitoneal injections of low-dose lipopolysaccharides (LPS) on four consecutive days, leading to mild sickness behaviour and temporary weight loss (Fig. 1a and Extended Data Fig. 1a). Three hours after the first LPS injection (1 × LPS), there was a pronounced increase in blood cytokine levels, but only modest increases in brain cytokines. Upon the second injection (2 × LPS), the blood levels of the pro-inflammatory cytokines IL-1β, TNF, IL-6, IL-12 and IFN-γ

were diminished compared to their levels after 1 × LPS, whereas IL-10 release was not reduced, indicating peripheral immune tolerance. In sharp contrast, brain cytokines were markedly increased by 2 × LPS injections, indicating a brain-specific training effect induced by the first LPS stimulus (Fig. 1b, c and Extended Data Fig. 2). Accordingly, a conspicuous morphological change in microglia occurred after 2 × LPS, whereas the number of activated (GFAP+) astrocytes increased only after 3 × LPS (Extended Data Fig. 1b–d). Notably, 4 × LPS virtually abolished TNF, IL-1β and IL-6 release in the brain whereas IL-10 remained elevated, indicating immune tolerance.

Next, we examined the contribution of microglia to immune memory in the brain using inducible CX3CR1-CreER (Cre) mice crossed with mouse lines carrying loxP-flanked genes, in which tamoxifen-induced Cre expression results in persistent recombination in long-lived microglia but not in short-lived myeloid cells, including blood monocytes[14]. We induced microglial knockout of either transforming growth factor-β-activated kinase 1 (Tak1, also known as Map3k7), which results in inhibition of the NF-κB, JNK and ERK1/2 pathways[14], or histone deacetylases-1 and -2 (Hdac1/2), two major regulators of epigenetic reprogramming and macrophage inflammatory responses[15]. As expected, tamoxifen-induced knockout of either Tak1 or Hdac1/2 did not alter the peripheral inflammatory response. Furthermore, brain cytokine levels were indistinguishable after 1 × LPS, but the training effect following 2 × LPS was virtually abolished in Cre+ mice. Notably, the cytokines showing the most pronounced training and tolerance effects (IL-1β, TNF, IL-6) were also the most affected by microglial gene knockout (Fig. 1b, c and Extended Data Fig. 2), indicating that immune memory in the brain is predominantly mediated by microglia. Moreover, after 1 × LPS, Cre+ and Cre− mice showed indistinguishable weight loss (Extended Data Fig. 1a) and

[1]German Center for Neurodegenerative Diseases (DZNE), Tübingen, Germany. [2]Department of Cellular Neurology, Hertie Institute for Clinical Brain Research, University of Tübingen, Tübingen, Germany. [3]Graduate School of Cellular and Molecular Neuroscience, University of Tübingen, Tübingen, Germany. [4]Department of Psychiatry and Psychotherapy, University Medical Center Göttingen, Göttingen, Germany. [5]Department for Systems Medicine and Epigenetics in Neurodegenerative Diseases, German Center for Neurodegenerative Diseases (DZNE), Göttingen, Germany. [6]Genomics and Immunoregulation, LIMES-Institute, University of Bonn, Bonn, Germany. [7]Bioinformatics Unit, German Center for Neurodegenerative Diseases (DZNE), Göttingen, Germany. [8]Institute of Neuropathology, Faculty of Medicine, University of Freiburg, Freiburg, Germany. [9]Platform for Single Cell Genomics and Epigenomics at the University of Bonn and the German Center for Neurodegenerative Diseases, Bonn, Germany. [10]Molecular Immunology in Neurodegeneration, German Center for Neurodegenerative Diseases (DZNE), Bonn, Germany. [11]BIOSS Centre for Biological Signalling Studies, University of Freiburg, Freiburg, Germany. [12]These authors contributed equally: Ann-Christin Wendeln, Karoline Degenhardt. *e-mail: jonas.neher@dzne.de
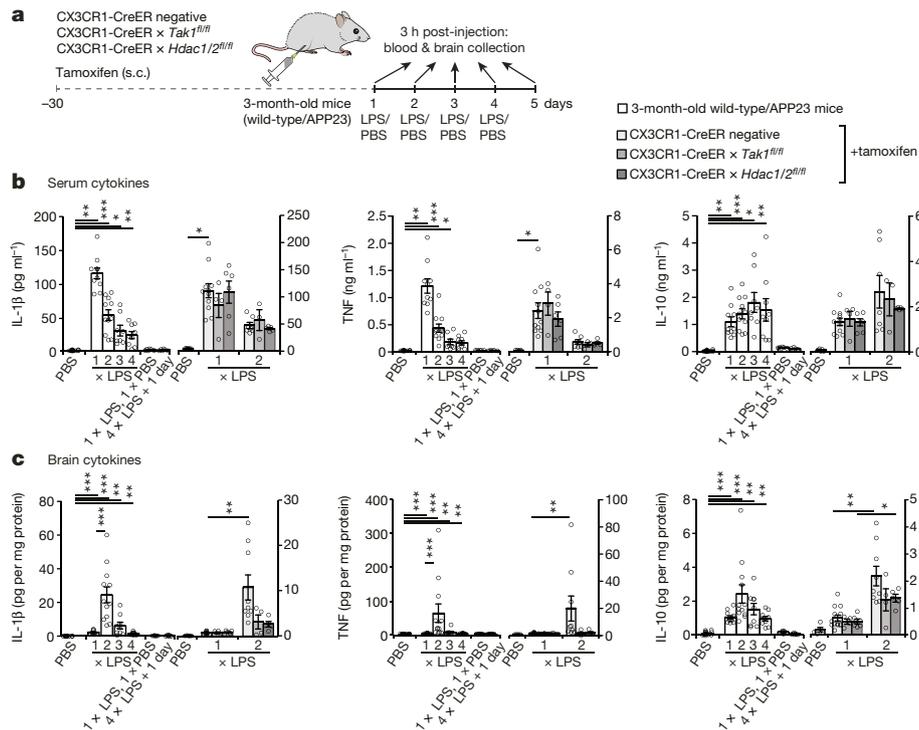
**Fig. 1 | Peripheral immune stimulation evokes immune memory in microglia. a**, Experimental approach. s.c., subcutaneous injection. **b**, Peripheral cytokine levels in wild-type or APP23 mice (white bars) and in mice with microglia-specific knockout of *Tak1* or *Hdac1/2* (coloured bars) following lipopolysaccharide (LPS) injections. Note that tolerance is induced with repeated injections. **c**, Brain cytokine levels, as in **b**. 2 × LPS amplifies IL-1β and TNF release in control mice, demonstrating immune training; tolerance occurs after 3 × LPS or 4 × LPS. Cytokines return to baseline within 24 h (1 × LPS, 1 × PBS and 4 × LPS + 1 day). Microglia-specific knockout of *Tak1* or *Hdac1/2* selectively prevents immune training in the brain. In **b** and **c**, *n* = 16, 11, 12, 9, 9, 7, 7, 5, 13, 4, 6, 9, 4, 5 from left to right. *$P < 0.05$, **$P < 0.01$, ***$P < 0.001$ for independent-samples median test with correction for multiple comparisons. Data are means ± s.e.m.

sickness behaviour (not shown); however, in animals with microglial *Tak1* knockout, sickness behaviour after 2 × LPS was noticeably alleviated (Supplementary Video 1).

After intraperitoneal injections, LPS was found in the blood but not in the brain, indicating that at this dose neither significant entry of LPS into the brain nor opening of the blood–brain barrier occurred, as previously reported[16]. The latter was confirmed by the absence of blood iron in the brain parenchyma. Also, using type 2 CC chemokine receptor (CCR2) reporter mice[17], we found no extravasation of circulating monocytes (Extended Data Fig. 1e–g), confirming that immune memory is mediated by brain-resident macrophages alone.

## Immune memory shapes neuropathology

Next, we analysed whether the training- and tolerance-inducing stimuli (1 × LPS and 4 × LPS, respectively) could lead to long-term alterations in brain immune responses and thereby modify disease pathogenesis. APP23 mice are a model of Alzheimer's disease pathology in which plaques of insoluble amyloid-β (Aβ) develop from 6 months of age. Amyloid plaques lead to activation of microglia[18], thereby providing a stimulus that should reveal microglial immune memory. We injected 3-month-old APP23 mice with either 1 × LPS or 4 × LPS, then analysed pathology 6 months later (Fig. 2a). Strikingly, 1 × LPS increased both plaque load and total Aβ levels compared to control animals, whereas 4 × LPS decreased both plaque load and Aβ levels (Fig. 2b), with plaque-associated neuritic damage correlating directly with plaque size in all treatment groups (Extended Data Fig. 3a–c). In addition, the protein levels of Aβ precursor protein (APP) and its cleavage products were indistinguishable among the groups, indicating equivalent Aβ generation (Extended Data Fig. 3d). Furthermore, neither the total number of microglia nor the number of microglia clustering around plaques was altered by LPS treatments (Fig. 2c), whereas the

number of activated (GFAP⁺) astrocytes decreased slightly in animals that received either 1 × LPS or 4 × LPS injections (Extended Data Fig. 3e). However, the brain levels of IL-1β, IL-6 and IL-12 were reduced in APP mice after 4 × LPS, whereas IL-10 was reduced in APP mice after 1 × LPS. By contrast, brain cytokine levels were not altered in wild-type littermate controls and baseline blood cytokine levels were unchanged in wild-type and APP animals. Furthermore, an additional LPS injection at 9 months of age caused peripheral cytokine responses that did not differ amongst LPS treatment groups in wild-type mice (Fig. 2d and Extended Data Fig. 4a–c). Thus, peripheral immune stimuli cause long-term alterations in the brain immune response and differentially affect Alzheimer's pathology.

To test for immune memory effects in a second disease model, we injected wild-type mice with 1 × LPS or 4 × LPS and induced focal brain ischaemia 1 month later. One day after ischaemia, neuronal damage and microglial numbers were indistinguishable amongst treatment groups (Fig. 3a), indicating that the initial ischaemic insult was unaffected by either 1 × LPS or 4 × LPS. However, the acute inflammatory response, which is driven by brain-resident cells early after ischaemia[12], differed, showing increased or decreased levels of IL-1β in mice injected with 1 × LPS or 4 × LPS, respectively. By contrast, the release of IL-10 was suppressed only by 1 × LPS (Fig. 3b), reminiscent of the results in APP mice (Fig. 2d). The levels of other brain cytokines and blood cytokines were indistinguishable amongst groups (Extended Data Fig. 5). Notably, 7 days after brain ischaemia, the volume of neuronal damage and microglial activation was strongly reduced in animals that received 4 × LPS but unaffected by 1 × LPS (Fig. 3c, d). These results confirm long-term modulation of brain immune responses and suggest persistent modification of stroke pathology following a tolerizing but not a training stimulus, possibly because the severity of the insult prevents its further exacerbation through amplification of the immune response.
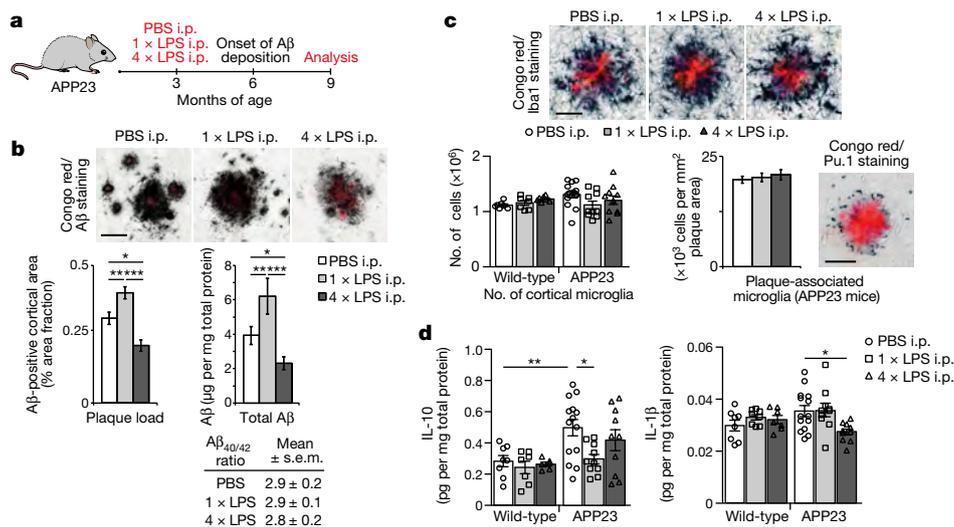
**Fig. 2 | Cerebral β-amyloidosis is altered after peripheral immune stimulation. a**, Experimental design. **b**, Analysis of cortical Aβ plaque load ($n = 22, 10, 10$ mice from left to right) and protein levels ($n = 14, 10, 10$ animals). **c, d**, Analysis of total cortical and plaque-associated microglia (**c**, $n = 7, 7, 7, 14, 10, 10$ mice) and cytokine levels of IL-10 and IL-1β (**d**) in wild-type and APP23 mice ($n = 8, 8, 7$ and $n = 14, 10, 10$ mice). i.p., intraperitoneal. Scale bar, 50 μm. *$P < 0.05$, **$P < 0.01$, ***$P < 0.001$ for one-way (**b**) and two-way ANOVA (**c, d**) with Tukey correction. Data are means ± s.e.m.

## Microglial molecular profiles

In vitro, immune memory in macrophages results from epigenetically mediated alterations in the enhancer repertoire, leading to transcriptional changes[3,19,20]. As our data indicate that acute immune memory in the brain is mediated predominantly by microglia, we isolated microglia by cell sorting (Extended Data Fig. 6) from 9-month-old animals stimulated with 1 × LPS or 4 × LPS at 3 months of age and performed chromatin immunoprecipitation for mono-methylation at lysine 4 of histone 3 (H3K4me1) and acetylation at lysine 27 of histone 3 (H3K27ac), which define active enhancers[19,20]. Thus, we identified 20,241 putative active enhancers across all conditions.

First, we focused on H3K4me1 marks, which should mark all enhancers activated in response to the first and/or second immune stimulus (as enhancers may lose H3K27ac after cessation of inflammation but retain H3K4me1 marks)[19,20]. Strikingly, H3K4me1 levels differed between control and LPS treatment groups both in wild-type and APP mice but also between mice treated with 1 × LPS or 4 × LPS (Extended Data Fig. 7b; Supplementary Table 1). For example, enhancers with increased H3K4me1 levels in microglia from wild-type

mice injected with 1 × LPS versus 4 × LPS showed enrichment for the thyroid hormone signalling pathway, including a putative enhancer for hypoxia inducible factor-1α (HIF-1α). Similarly, enhancers with higher H3K4me1 levels in APP mice injected with 1 × LPS versus 4 × LPS were enriched for the HIF-1 signalling pathway. On the other hand, APP mice treated with 4 × LPS showed increased H3K4me1 levels in putative enhancers related to phagocytic function (Table 1a). Notably, we found no pathway enrichment when comparing H3K4me1 levels in microglia from APP and wild-type control mice (Table 1a), indicating that H3K4me1 levels were altered predominantly in response to LPS stimulation.

Next, we analysed enhancer activation by testing for differential regulation of H3K27ac levels. In line with the requirement of an acute stimulus for H3K27ac deposition[19], differential enhancer activation was more pronounced in APP mice (where amyloid plaques activate microglia) than in wild-type mice ($190 ± 18$ in APP, $69 ± 5$ in wild-type; Extended Data Fig. 7e; Supplementary Table 2). For example, differentially regulated H3K27ac levels in microglia from APP mice treated with 1 × LPS versus control APP mice were enriched for the
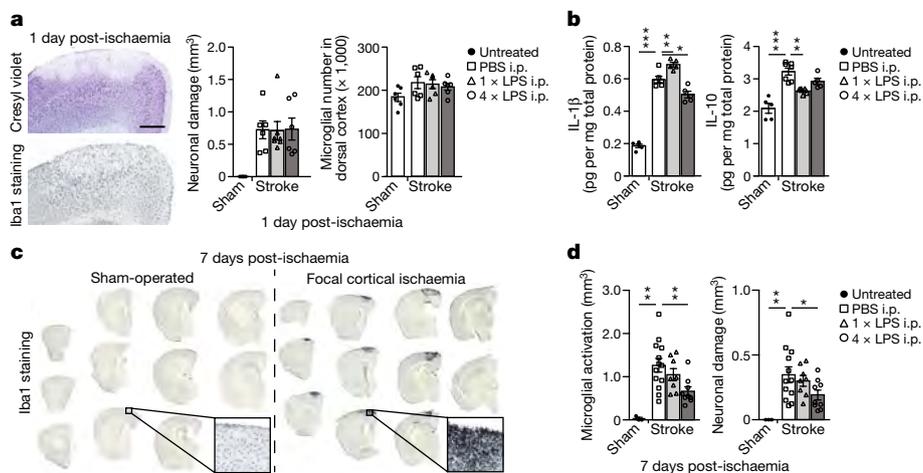


**Fig. 3 | Stroke pathology is altered after peripheral immune stimulation.** Pathological features of brain ischaemia induced one month after intraperitoneal (i.p.) injection with 1 × LPS or 4 × LPS. **a**, Neuronal damage (cresyl violet, $n = 6, 6, 7, 6$ mice from left to right) and number of microglia (Iba1-positive, $n = 6, 6, 6, 6$ mice). **b**, Cytokine profiles 1 day post-ischaemia ($n = 5, 7, 5, 5$ mice). **c, d**, Overview of microglial activation in the infarct (**c**) and quantification of neuronal damage and microglial activation (**d**) 7 days post-ischaemia ($n = 3, 13, 8, 9$ mice). Scale bar, 500 μm. *$P < 0.05$, **$P < 0.01$, ***$P < 0.001$ for one-way ANOVA with Tukey correction. Data are means ± s.e.m.

**Table 1 | The microglial enhancer repertoire 6 months after immune stimulation**

**a** KEGG pathway enrichment of differentially regulated H3K4me1 regions (threshold ≥ 1.5-fold)

| | Condition 1 | Condition 2 | Increased in condition 1 | logP | Increased in condition 2 | logP |
|---|---|---|---|---|---|---|
| | APP PBS | Wild-type PBS | | | | |
| **Wild-type** | 1 × LPS | PBS | Renal cell carcinoma | −10 | | |
| | | | Focal adhesion | −6 | | |
| | | | MAPK signalling pathway | −5 | | |
| | | | Chemokine signalling pathway | −5 | | |
| | 4 × LPS | PBS | Endocytosis | −7 | PI3K-Akt signalling pathway | −4 |
| | | | Proteoglycans in cancer | −5 | | |
| | | | MAPK signalling pathway | −5 | | |
| | | | Colorectal cancer | −5 | | |
| | 1 × LPS | 4 × LPS | Proteoglycans in cancer | −6 | B cell receptor signalling pathway | −8 |
| | | | Thyroid hormone signalling pathway | −4 | MAPK signalling pathway | −8 |
| | | | | | FcγR-mediated phagocytosis | −8 |
| | | | | | Leishmaniasis | −7 |
| | | | | | Legionellosis | −5 |
| | | | | | Toll-like receptor signalling pathway | −5 |
| | | | | | Focal adhesion | −5 |
| | | | | | TNF signalling pathway | −5 |
| | | | | | Rap1 signalling pathway | −5 |
| | | | | | Osteoclast differentiation | −4 |
| **APP** | 1 × LPS | PBS | Transcriptional misregulation in cancer | −8 | | |
| | | | Leukocyte transendothelial migration | −5 | | |
| | | | Glycosphingolipid biosynthesis | −5 | | |
| | 4 × LPS | PBS | Osteoclast differentiation | −11 | | |
| | | | Leukocyte transendothelial migration | −9 | | |
| | | | Cytokine–cytokine receptor interaction | −6 | | |
| | | | Adherens junction | −6 | | |
| | | | FcγR-mediated phagocytosis | −6 | | |
| | | | Rap1 signalling pathway | −5 | | |
| | | | MAPK signalling pathway | −5 | | |
| | | | Endocytosis | −5 | | |
| | | | TGF-β signalling pathway | −4 | | |
| | | | Transcriptional misregulation in cancer | −4 | | |
| | | | Chemokine signalling pathway | −4 | | |
| | 1 × LPS | 4 × LPS | Salmonella infection | −6 | Rap1 signalling pathway | −10 |
| | | | Chagas disease | −5 | Osteoclast differentiation | −8 |
| | | | HIF-1 signalling pathway | −5 | Insulin signalling pathway | −8 |
| | | | Toxoplasmosis | −5 | Chemokine signalling pathway | −7 |
| | | | | | MAPK signalling pathway | −6 |
| | | | | | Glycosaminoglycan biosynthesis | −5 |

**b** KEGG pathway enrichment of differentially regulated H3K27ac regions (threshold ≥ 1.5-fold)

| | Condition 1 | Condition 2 | Increased in condition 1 | logP | Increased in condition 2 | logP |
|---|---|---|---|---|---|---|
| | APP PBS | Wild-type PBS | Thyroid hormone signalling pathway | −6 | | |
| | | | mTOR signalling pathway | −5 | | |
| **Wild-type** | 1 × LPS | PBS | | | | |
| | 4 × LPS | PBS | | | | |
| | 1 × LPS | 4 × LPS | Transcriptional misregulation in cancer | −5 | Transcriptional misregulation in cancer | −5 |
| | | | | | Ras signalling pathway | −4 |
| **APP** | 1 × LPS | PBS | HIF-1 signalling pathway | −8 | MAPK signalling pathway | −7 |
| | | | Thyroid hormone signalling pathway | −7 | | |
| | | | Carbohydrate digestion and absorption | −6 | | |
| | | | Osteoclast differentiation | −5 | | |
| | | | AMPK signalling pathway | −5 | | |
| | | | Chronic myeloid leukaemia | −5 | | |
| | 4 × LPS | PBS | Rap1 signalling pathway | −5 | MAPK signalling pathway | −9 |
| | | | | | Osteoclast differentiation | −6 |
| | | | | | Thyroid hormone synthesis | −5 |
| | | | | | Chemokine signalling pathway | −4 |
| | 1 × LPS | 4 × LPS | Osteoclast differentiation | −12 | | |
| | | | Bacterial invasion of epithelial cells | −11 | | |
| | | | Toll-like receptor signalling pathway | −10 | | |
| | | | Ras signalling pathway | −9 | | |
| | | | Thyroid hormone signalling pathway | −9 | | |
| | | | FcγR-mediated phagocytosis | −9 | | |
| | | | mTOR signalling pathway | −8 | | |
| | | | Rap1 signalling pathway | −8 | | |
| | | | Regulation of actin cytoskeleton | −8 | | |
| | | | Carbohydrate digestion and absorption | −8 | | |
| | | | Phosphatidylinositol signalling system | −7 | | |
| | | | Chemokine signalling pathway | −7 | | |
| | | | Jak-STAT signalling pathway | −7 | | |
| | | | Focal adhesion | −7 | | |
| | | | Transcriptional misregulation in cancer | −6 | | |
| | | | Oestrogen signalling pathway | −6 | | |
| | | | TNF signalling pathway | −6 | | |
| | | | HIF-1 signalling pathway | −6 | | |
| | | | PI3K-Akt signalling pathway | −6 | | |
| | | | Chronic myeloid leukaemia | −6 | | |
| | | | Acute myeloid leukaemia | −5 | | |

Pathway enrichment of putative enhancers (with Benjamini–Hochberg correction) with differentially regulated H3K4me1 and H3K27ac levels (based on nearest gene; cumulative Poisson $P < 0.0001$). $n = 2$ replicates (8–10 mice per replicate).
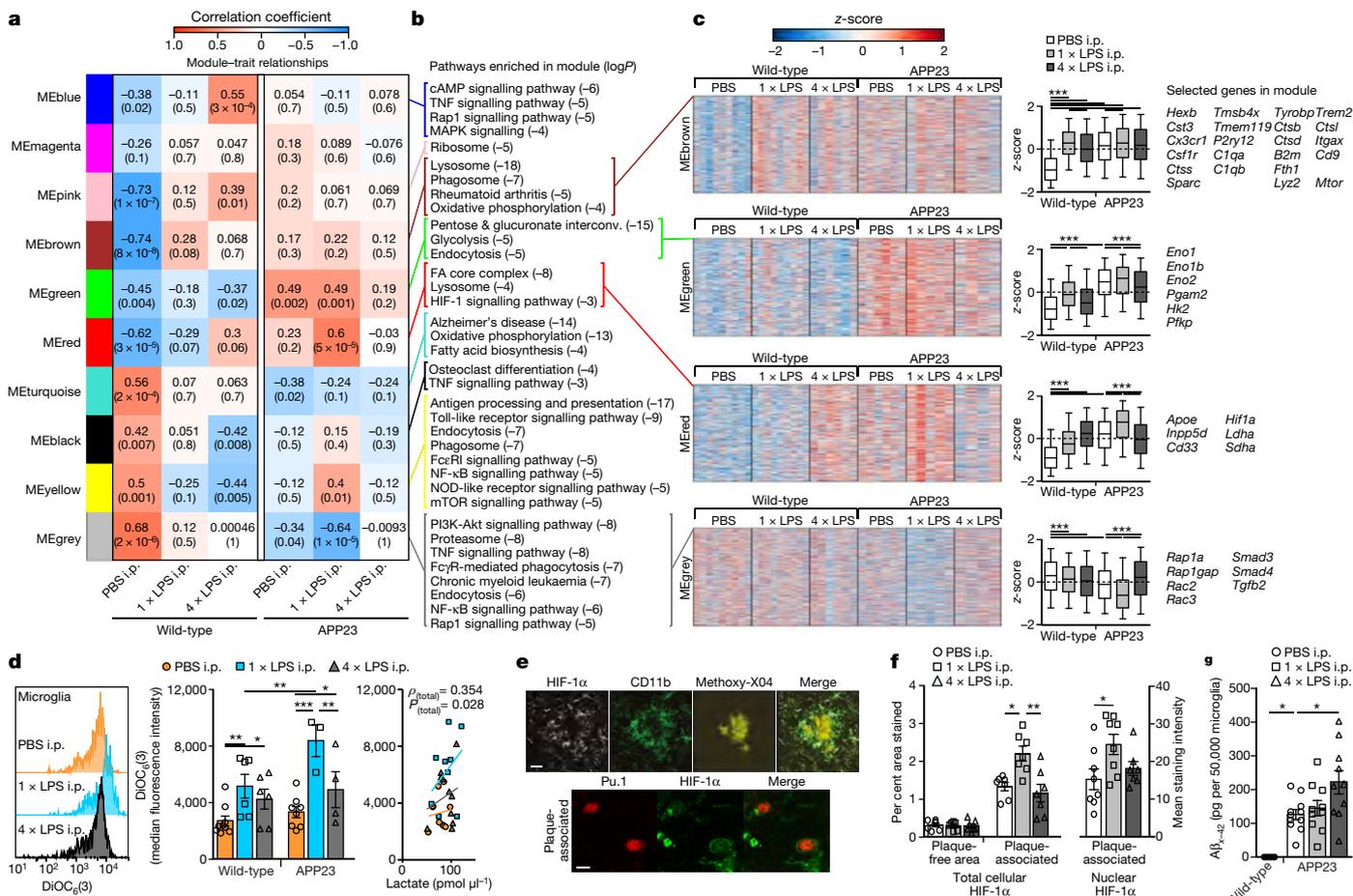
**Fig. 4 | Microglial gene expression and function 6 months after immune stimulation. a**, WGCNA (top, correlation coefficient; bottom, *P* value; *n* = 9, 9, 6, 6, 5, 4 mice from left to right). **b**, Selected KEGG pathways enriched in modules. **c**, Heatmaps of genes within modules, *z*-scores (boxplot whisker, 5th–95th percentile; *n* = 1,601, 990, 949 and 3,543 genes in modules) and selected genes. **d**, Microglial mitochondrial membrane potential (left, middle; *n* = 9, 6, 6, 8, 3, 4 mice) and Pearson's correlation with lactate release (right;

*n* = 11, 10, 10 mice). **e**, Top, staining for HIF-1α, microglia (CD11b) and amyloid plaques (Methoxy-X04); bottom, staining for HIF-1α and microglial nuclei (Pu.1; single confocal plane) in brain sections from 9-month-old mice. Scale bars, 20 μm (top); 5 μm (bottom). **f**, Total cellular (*n* = 7, 7, 7 mice) and nuclear (*n* = 8, 8, 7 mice) HIF-1α staining intensity. **g**, Microglial Aβ content (*n* = 5, 11, 10, 10 mice). *P < 0.05, **P < 0.01, ***P < 0.001 for one-way ANOVA with Tukey correction. Data are means ± s.e.m.

HIF-1 signalling pathway, with enhancer regions also being enriched for HIF-1α binding motifs (Table 1b and Extended Data Fig. 8), in line with changes in H3K4me1 levels (Table 1a) and the reported key role of HIF-1α in trained immunity and macrophage inflammatory responses[4,21].

Active enhancers in microglia from 4 × LPS-treated APP mice versus control APP mice showed enrichment only for the Rap1 signalling pathway, which has been implicated in phagocytosis of opsonized targets[22,23], again matching changes in H3K4me1 levels (Table 1). Strikingly, comparison of microglia from APP mice that received the training- (1 × LPS) or tolerance-inducing (4 × LPS) stimuli showed no pathway enrichment for active enhancers in mice injected with 4 × LPS, whereas enhancers in 1 × LPS-treated mice were enriched for a large number of inflammation-related pathways, highlighting the differential effects of the two immune memory states. Finally, comparison of microglia from vehicle-treated wild-type and APP mice demonstrated a small number of differentially activated enhancers with enrichment for the thyroid hormone signalling pathway (including a putative active enhancer for *Hif1a*) and the mTOR signalling pathway (Table 1b), indicating that microglia are also epigenetically reprogrammed in response to brain pathology alone.

We next examined microglial mRNA levels under the same conditions to determine whether epigenetic alterations were reflected in gene expression (Supplementary Table 3). First, we determined the concordance between 772 enhancers with significantly increased or decreased

H3K27ac levels (Supplementary Table 2) and the direction of change in the expression of their nearest gene. Indeed, there was a significant (albeit modest) concordance between alterations in H3K27ac levels and gene expression (median concordance of pairwise comparisons, 58%; *P* = 0.03). This suggested that gene expression is directly affected by the microglial active enhancer repertoire. Accordingly, weighted gene correlation network analysis (WGCNA[24]) revealed striking parallels to epigenetic changes (Fig. 4a–c and Supplementary Table 4). For example, the red module (MEred; Fig. 4a) contained the *Hif1a* gene, showed enrichment for the HIF-1 signalling pathway and correlated strongly with the 1 × LPS-injected APP group. Furthermore, gene expression in MEred was upregulated in APP versus wild-type control mice and further increased by 1 × LPS, but downregulated by 4 × LPS.

HIF-1α activation in inflammatory-stimulated macrophages can occur downstream of mitochondrial hyperpolarization; enhanced HIF-1α signalling in turn promotes glycolysis, measurable as lactate release[25]. Accordingly, the green module (MEgreen; Fig. 4a), which correlated positively with control and 1 × LPS-treated APP groups but negatively with control and 4 × LPS-treated wild-type groups, was found to be enriched in genes of the glycolysis pathway. Microglial gene expression in MEgreen was upregulated in APP versus wild-type control mice and further increased in APP mice by 1 × LPS but decreased in mice that received 4 × LPS. Therefore, we analysed mitochondrial membrane potential and lactate release in microglia. Strikingly, microglia from 1 × LPS-treated APP mice showed strongly increased

mitochondrial membrane potential, which correlated positively with the release of lactate (Fig. 4d), functionally corroborating the epigenetic and transcriptional alterations in trained microglia. Additionally, immunostaining confirmed an increase in protein levels of HIF-1α in plaque-associated microglia; these levels were further increased in 1 × LPS-treated APP mice (Fig. 4e, f). Thus, HIF-1α signalling and a metabolic switch to glycolysis are activated in response to cerebral β-amyloid deposition, and are enhanced by immune training but reduced by immune tolerance in microglia.

In contrast to MEred and MEgreen, the MEgrey module correlated positively with the control wild-type but negatively with the control APP and 1 × LPS-treated APP groups. Compared to wild-type controls, microglial gene expression in MEgrey was downregulated in APP control animals and further decreased by 1 × LPS, but showed unchanged levels in APP mice injected with 4 × LPS compared with wild-type controls (Fig. 4a–c). Notably, MEgrey was enriched for phagocytosis-related pathways, including the Rap1 signalling pathway (Fig. 4a–c), again reflecting epigenetic changes (Table 1). We therefore tested whether phagocytosis of Aβ was enhanced in 4 × LPS-treated APP mice. Indeed, microglial Aβ content was increased around 1.75-fold in these mice compared to APP control mice (Fig. 4g), providing further functional validation of the microglial enhancer repertoire and gene expression profiles.

Recent data have indicated that context-specific microglial phenotypes exist, for example, disease-associated microglia (DAM[26]) and the microglial neurodegenerative phenotype (MGnD[27]). Notably, the MEbrown module, which was upregulated by both LPS treatments in wild-type mice as well as in all APP groups, contained a number of homeostatic microglial genes (for example, *Hexb*, *Cx3cr1* and *Csf1r*) but also all of the stage 1 DAM core genes except *Apoe*, as well as four of twelve stage 2 core genes[26] (Fig. 4c). Interestingly, the gene encoding ApoE, which may be crucial for promoting a detrimental microglial phenotype[27,28], was found in the same module (MEred) as *Hif1a*. MEred also contained other genes genetically linked to risk for Alzheimer's disease, namely *Cd33* and *Inpp5d*[29], suggesting that HIF-1α may also be a detrimental modulator of Alzheimer's disease pathology.

The epigenetic landscape of microglia has been described only under homeostatic conditions[30–32]. Our data now demonstrate epigenetic modifications in microglia in response to peripheral immune stimulation but also as a result of cerebral β-amyloidosis, including activation of the HIF-1α and mTOR pathways, and leading to transcriptional and functional alterations. Although the global epigenetic and transcriptional changes were relatively modest, they are likely to have been driven by a small number of microglia that received the required secondary immune stimulation, as evidenced for example by increased levels of HIF-1α in plaque-associated microglia (Fig. 4). mTOR activation is a well-known event in early Alzheimer's disease[33] and was recently shown in microglia, where it activated HIF-1α and glycolysis to sustain microglial energy demand in models of Alzheimer's disease pathology[34]. Our data now indicate that mTOR activation may be mediated by epigenetic microglial reprogramming in response to cerebral β-amyloidosis and that HIF-1α signalling downstream of mTOR could be a detrimental event, because augmentation or suppression of HIF-1α signalling occurred concomitantly with aggravated or alleviated Aβ deposition, respectively.

We here provide evidence of both immune training and tolerance in microglia and demonstrate their impact on neuropathology for the first time. While we cannot completely exclude the possibility that other cell-types contribute to immune memory and modulation of pathology in the brain, microglial-specific gene knockout of *Tak1* or *Hdac1/2* virtually abolished immune training (Fig. 1), indicating that microglia are likely to be the major effectors of immune memory. Notably, in our experiments, the effects of immune memory mostly became apparent following a secondary inflammatory stimulus, corroborating the concept of innate immune memory[1,3]. However, while in the periphery training may be beneficial owing to enhanced pathogen elimination[7,35,36], and tolerance may be detrimental owing to higher rates of infection resulting from immune suppression[5], we found that training promotes, while tolerance alleviates, neuropathology. This is consistent with the beneficial effects of preventing microglial pro-inflammatory responses in models of Alzheimer's disease pathology and stroke[12,37] and the worsening of cerebral β-amyloidosis in response to pro-inflammatory peripheral stimuli in animal models[38]. Similarly, immune training has recently been described in epithelial stem cells, where it promotes wound healing but may also underlie autoimmune disorders[39]. Thus, immune memory in the brain could conceivably affect the severity of any neurological disease that presents with an inflammatory component, but this will need to be studied for each individual condition.

Our data provide proof-of-principle for innate immune memory in microglia, and while our different LPS injection paradigms may not necessarily model physiological stimuli, we found that individual cytokines applied peripherally may also elicit immune memory effects in the brain (Extended Data Fig. 9). These results suggest that a wide variety of immune challenges may induce microglial immune memory and provide a possible mechanism for LPS-induced immune memory in the brain. It will be crucial to determine which other stimuli may lead to long-term modulation of microglial responses and thereby contribute to the severity of many neurological diseases.

## Online content

Any Methods, including any statements of data availability and Nature Research reporting summaries, along with any additional references and Source Data files, are available in the online version of the paper at https://doi.org/10.1038/s41586-018-0023-4.

1. Netea, M. G., Latz, E., Mills, K. H. G. & O'Neill, L. A. J. Innate immune memory: a paradigm shift in understanding host defense. *Nat. Immunol.* **16**, 675–679 (2015).
2. Netea, M. G. et al. Trained immunity: A program of innate immune memory in health and disease. *Science* **352**, aaf1098 (2016).
3. Saeed, S. et al. Epigenetic programming of monocyte-to-macrophage differentiation and trained innate immunity. *Science* **345**, 1251086 (2014).
4. Cheng, S. C. et al. mTOR- and HIF-1α-mediated aerobic glycolysis as metabolic basis for trained immunity. *Science* **345**, 1250684 (2014).
5. Biswas, S. K. & Lopez-Collazo, E. Endotoxin tolerance: new mechanisms, molecules and clinical significance. *Trends Immunol.* **30**, 475–487 (2009).
6. Novakovic, B. et al. β-Glucan reverses the epigenetic state of LPS-induced immunological tolerance. *Cell* **167**, 1354–1368 (2016).
7. Kleinnijenhuis, J. et al. Bacille Calmette-Guerin induces NOD2-dependent nonspecific protection from reinfection via epigenetic reprogramming of monocytes. *Proc. Natl Acad. Sci. USA* **109**, 17537–17542 (2012).
8. Tay, T. L. et al. A new fate mapping system reveals context-dependent random or clonal expansion of microglia. *Nat. Neurosci.* **20**, 793–803 (2017).
9. Füger, P. et al. Microglia turnover with aging and in an Alzheimer's model via long-term in vivo single-cell imaging. *Nat. Neurosci.* **20**, 1371–1376 (2017).
10. Prinz, M. & Priller, J. Microglia and brain macrophages in the molecular age: from origin to neuropsychiatric disease. *Nat. Rev. Neurosci.* **15**, 300–312 (2014).
11. Heneka, M. T., Kummer, M. P. & Latz, E. Innate immune activation in neurodegenerative disease. *Nat. Rev. Immunol.* **14**, 463–477 (2014).
12. Iadecola, C. & Anrather, J. The immunology of stroke: from mechanisms to translation. *Nat. Med* **17**, 796–808 (2011).
13. Perry, V. H., Cunningham, C. & Holmes, C. Systemic infections and inflammation affect chronic neurodegeneration. *Nat. Rev. Immunol.* **7**, 161–167 (2007).
14. Goldmann, T. et al. A new type of microglia gene targeting shows TAK1 to be pivotal in CNS autoimmune inflammation. *Nat. Neurosci.* **16**, 1618–1626 (2013).
15. Datta, M. et al. Histone deacetylases 1 and 2 regulate microglia function during development, homeostasis, and neurodegeneration in a context-dependent manner. *Immunity* http://www.cell.com/immunity/fulltext/S1074-7613(18)30075-X (2018).
16. Banks, W. A. & Robinson, S. M. Minimal penetration of lipopolysaccharide across the murine blood-brain barrier. *Brain Behav. Immun.* **24**, 102–109 (2010).
17. Saederup, N. et al. Selective chemokine receptor usage by central nervous system myeloid cells in CCR2-red fluorescent protein knock-in mice. *PLoS One* **5**, e13693 (2010).
18. Sturchler-Pierrat, C. et al. Two amyloid precursor protein transgenic mouse models with Alzheimer disease-like pathology. *Proc. Natl Acad. Sci. USA* **94**, 13287–13292 (1997).

19. Ostuni, R. et al. Latent enhancers activated by stimulation in differentiated cells. *Cell* **152**, 157–171 (2013).
20. Kaikkonen, M. U. et al. Remodeling of the enhancer landscape during macrophage activation is coupled to enhancer transcription. *Mol. Cell* **51**, 310–325 (2013).
21. Cramer, T. et al. HIF-1α is essential for myeloid cell-mediated inflammation. *Cell* **112**, 645–657 (2003).
22. Caron, E., Self, A. J. & Hall, A. The GTPase Rap1 controls functional activation of macrophage integrin αMβ2 by LPS and other inflammatory mediators. *Curr. Biol.* **10**, 974–978 (2000).
23. Li, Y. et al. Rap1a null mice have altered myeloid cell functions suggesting distinct roles for the closely related Rap1a and 1b proteins. *J. Immunol.* **179**, 8322–8331 (2007).
24. Langfelder, P. & Horvath, S. WGCNA: an R package for weighted correlation network analysis. *BMC Bioinformatics* **9**, 559 (2008).
25. Mills, E. L. et al. Succinate dehydrogenase supports metabolic repurposing of mitochondria to drive inflammatory macrophages. *Cell* **167**, 457–470 (2016).
26. Keren-Shaul, H. et al. A unique microglia type associated with restricting development of Alzheimer's disease. *Cell* **169**, 1276–1290 (2017).
27. Krasemann, S. et al. The TREM2-APOE pathway drives the transcriptional phenotype of dysfunctional microglia in neurodegenerative diseases. *Immunity* **47**, 566–581 (2017).
28. Shi, Y. et al. ApoE4 markedly exacerbates tau-mediated neurodegeneration in a mouse model of tauopathy. *Nature* **549**, 523–527 (2017).
29. Lambert, J. C. et al. Meta-analysis of 74,046 individuals identifies 11 new susceptibility loci for Alzheimer's disease. *Nat. Genet.* **45**, 1452–1458 (2013).
30. Gosselin, D. et al. Environment drives selection and function of enhancers controlling tissue-specific macrophage identities. *Cell* **159**, 1327–1340 (2014).
31. Lavin, Y. et al. Tissue-resident macrophage enhancer landscapes are shaped by the local microenvironment. *Cell* **159**, 1312–1326 (2014).
32. Gosselin, D. et al. An environment-dependent transcriptional network specifies human microglia identity. *Science* **1617**, eaal3222 (2017).
33. Wang, C. et al. Targeting the mTOR signaling network for Alzheimer's disease therapy. *Mol. Neurobiol.* **49**, 120–135 (2014).
34. Ulland, T. K. et al. TREM2 maintains microglial metabolic fitness in Alzheimer's disease. *Cell* **170**, 649–663 (2017).
35. Kaufmann, E. et al. BCG educates hematopoietic stem cells to generate protective innate immunity against tuberculosis. *Cell* **172**, 176–190 (2018).
36. Arts, R. J. W. et al. BCG vaccination protects against experimental viral infection in humans through the induction of cytokines associated with trained immunity. *Cell Host Microbe* **23**, 89–100 (2018).
37. Heneka, M. T., Golenbock, D. T. & Latz, E. Innate immunity in Alzheimer's disease. *Nat. Immunol.* **16**, 229–236 (2015).
38. O'Banion, M. K. Does peripheral inflammation contribute to Alzheimer disease? Evidence from animal models. *Neurology* **83**, 480–481 (2014).
39. Naik, S. et al. Inflammatory memory sensitizes skin epithelial stem cells to tissue damage. *Nature* **550**, 475–480 (2017).

**Author contributions** K.D., A.-C.W., J.W., L.M.H., K.W., A.S., T.B, O.S., M.D. and J.J.N. performed microglial isolation, in vivo and ex vivo experiments and histological/biochemical analyses. M.G., L.K., G.J., T.P.C., V.C., R.I., C.K., A.F., M.B., T.U., J.L.S. and J.J.N. performed ChIP–seq and RNA-seq analyses. J.J.N conceived the study and coordinated the experiments together with M.J., A.F., M.P., M.B., J.L.S. and M.S. J.J.N. wrote the manuscript, with contributions from all authors.

**Competing interests** The authors declare no competing interests.

**Additional information**
**Extended data** is available for this paper at https://doi.org/10.1038/s41586-018-0023-4.
**Supplementary information** is available for this paper at https://doi.org/10.1038/s41586-018-0023-4.
**Reprints and permissions information** is available at http://www.nature.com/reprints.
**Correspondence and requests for materials** should be addressed to J.J.N.
**Publisher's note:** Springer Nature remains neutral with regard to jurisdictional claims in published maps and institutional affiliations.

## METHODS

**Mice.** For all experiments, 3-month-old hemizygous APP23 transgenic (C57BL/6J-Tg(Thy1-APP$_{K670N;M671L}$)23), APP23 transgene-negative littermate or C57BL/6J (wild-type) mice (Jackson Laboratory) or type 2 CC chemokine receptor (CCR2) reporter mice (kindly provided by R. Ransohoff, Boston) were used.

For experiments analysing immune responses after acute LPS and cytokine stimulation (see below), both male and female mice were used. For microglia-specific gene knockouts, CX3CR1-CreER animals were crossed with *Tak1*$^{fl/fl}$ animals and Cre recombinase expression was induced by subcutaneous tamoxifen injections as previously described[14]. Similarly, microglial-specific knockout of *Hdac1/2* was achieved after crossing CX3CR1-CreER animals (kindly provided by S. Jung (Weizman Institute, Rehovot)) with a *Hdac1/2*$^{fl/fl}$ line (kindly provided by P. Matthias (FMI Basel)). Both *Tak1*$^{fl/fl}$ and *Hdac1/2*$^{fl/fl}$ mice were injected with tamoxifen at 2–3 months of age and were incubated for four weeks without further treatment. Tamoxifen-injected CX3CR1-Cre-negative littermates were used as controls (because responses in CX3CR1-Cre-negative mice were indistinguishable in *Hdac1/2*$^{fl/fl}$ and *Tak1*$^{fl/fl}$ lines, pooled data are shown in Fig. 1).

As there is a significant gender effect on the pathology of both brain ischaemia and cerebral β-amyloidosis[40,41], only female mice were used for the analyses of brain pathology. APP23 mice express a transgene consisting of human APP with the KM670/671NL mutation under the Thy-1 promoter, and have been backcrossed with C57BL/6J mice for more than 20 generations. Female mice develop cerebral Aβ lesions in the neocortex at around 6 months of age[18].

Animals were maintained under specific pathogen-free conditions. All experiments were performed in accordance with the veterinary office regulations of Baden-Württemberg (Germany) and were approved by the Ethical Commission for animal experimentation of Tübingen and Freiburg, Germany.

**Peripheral immune stimulation.** Three-month-old mice were randomly assigned to treatment groups and were injected intraperitoneally (i.p.) with bacterial lipopolysaccharides (LPS from *Salmonella enterica* serotype typhimurium, Sigma) at a daily dose of 500 μg per kg bodyweight. Animals received either four LPS injections on four consecutive days (4 × LPS), a single LPS injection followed by three vehicle injections on the following three days (1 × LPS) or four vehicle injections (PBS). Acute stimulation showed indistinguishable cytokine responses in wild-type and APP23 transgenic animals; Fig. 1 shows the pooled data from both genotypes (see Extended Data Fig. 2 for data separated by genotype). Furthermore, as cytokine responses were indistinguishable in animals treated with one, two, three or four injections of PBS, pooled data from all time points are shown.

For peripheral cytokine treatments, recombinant mouse cytokines (TNF, IL-10; PeproTech) were aliquoted as per the manufacturer's instructions and stored at −80 °C until use. To determine whether a long-term change in the brain's immune response (training or tolerance) occurred after peripheral cytokine injection, mice were treated on four consecutive days with 0.1 μg per g bodyweight IL-10 or once with 0.1 or 0.2 μg per g bodyweight TNFα. Control mice received four vehicle injections (PBS). Four weeks later, cytokine- and control-treated mice were injected with LPS (1 μg per g bodyweight) or PBS, and were killed 3 h after the injection.

At the specified time-points, animals were deeply anaesthetized using sedaxylan and ketamine (64 mg/kg and 472 mg/kg), blood was collected from the right ventricle of the heart and animals were transcardially perfused with ice-cold PBS through the left ventricle. The brain was removed and sagitally separated into the two hemispheres, which were either fixed in 4% paraformaldehyde (PFA) or fresh-frozen on dry ice. Fresh-frozen hemispheres were homogenized using a Precellys lysing kit and machine at 10 or 20% (w/v) in homogenization buffer (50 mM Tris pH 8, 150 mM NaCl, 5 mM EDTA) containing phosphatase and protease inhibitors (Pierce). Fixed hemispheres were kept in 4% PFA for 24 h, followed by cryoprotection in 30% sucrose in PBS, subsequently frozen in 2-methylbutane and coronally sectioned at 25 μm using a freezing-sliding microtome (Leica).

**Focal brain ischaemia.** For the induction of a focal cortical stroke, we modified existing models of endothelin-1 (ET-1)-induced brain ischaemia[42] to avoid traumatic injury to the brain. Under anaesthesia and analgesia (fentanyl, midazolam and medetomidin: 0.05, 5 and 0.5 mg/kg bodyweight), 3-month-old mice were fixed in a stereotactic frame and a circular piece of skull was removed (5 mm diameter, centred on Bregma as described[43]). The dura mater was carefully removed with the help of a microhook (Fine Science Tools) and 5 μl ET-1 (Bachem; 64 μM) in Hanks buffered salt solution (Invitrogen) or vehicle solution was topically applied to the cortex and incubated for 10 min. The craniotomy was then covered with a 5-mm glass coverslip, which was fixed in place with dental cement (Hybond), the skin was sutured, then the mice received antidote (flumazenil and atipamezol: 0.5 and 2.5 mg per kg bodyweight) and their health was monitored. Control mice underwent the same surgical procedure with application of vehicle solution to the cortex. After 4 weeks, animals were deeply anaesthetized and perfused as described above.

**Western blotting analysis.** For western blotting, total brain homogenates were sonicated three times for 5 s (LabSonic, B. Braun Biotech), and the protein levels of the brain homogenates were quantified with a microplate bicinchoninic acid (BCA) assay (Pierce) and adjusted accordingly. Samples were then analysed on NuPage Bis-Tris gels (Invitrogen) using standard procedures. Proteins were transferred to nitrocellulose membranes, blocking was performed with 5% milk in PBS containing 0.05% Tween (PBST) for 1 h and blots were incubated with mouse anti-Aβ (6E10; 1:1,000, Covance) in PBST overnight at 4 °C. Membranes were then probed with secondary HRP-labelled antibodies (1:20,000, Jackson ImmunoLaboratories). Protein bands were detected using chemiluminescent peroxidase substrate (ECL prime, GE Healthcare). Densitometric values of the protein band intensities were analysed with the software package Aida v.4.27 and normalized to GAPDH intensities.

**Immunostaining.** Immunohistochemical staining was performed on free-floating sections using either Vectastain Elite ABC kits (Vector laboratories) or fluorescent secondary antibodies (Jackson Immunolaboratories). Unless otherwise noted, brain sections were blocked for 1 h with 5% normal serum of the secondary antibody species, followed by primary antibody incubation overnight at 4 °C. Primary antibodies used were: rabbit anti-Pu.1 (1:1,000, Cell Signalling), rabbit anti-Iba1 (1:1,000; Wako; catalogue no. 019-19741), rabbit anti-GFAP (1:500, Biozol; catalogue no. Z0334), rabbit anti-Aβ (CN3; 1:2,000)[44], mouse anti-HIF-1α (1:500; Novus Biologicals, catalogue no. NB100-105, clone H1alpha67), rat anti-CD11b (1:2,000; Millipore, catalogue no. MAB1387Z), rabbit anti-APP (antibody 5313 to the ectodomain of APP, 1:750; kindly provided by C. Haass, DZNE Munich). Sections were then washed and incubated with secondary antibodies. Cresyl violet and Congo red staining was conducted according to standard procedures. Fluorescent plaque staining was achieved using Methoxy-X04 (4% vol of 10 mg/ml methoxy-X04 in DMSO, and 7.7% vol CremophorEL in 88.3% vol PBS) for 20 min at room temperature.

Images were acquired on an Axioplan 2 microscope with Axioplan MRm and AxioVision 4.7 software (Carl Zeiss). Fluorescent images were acquired using a LSM 510 META (Axiovert 200 M) confocal microscope with an oil immersion 63 × /1.4NA objective and LSM software 4.2 (Carl Zeiss), using sequential excitation of fluorophores. Maximum-intensity projections were generated using IMARIS 8.3.1 software (Bitmap).

For quantitative comparisons, sections from all groups were stained in parallel and analysed with the same microscope settings by an observer blinded to the treatment groups. To quantify the intensity of total microglial HIF-1α staining, high-resolution bright-field images were acquired using fixed camera exposure time and lamp intensity and subsequently analysed with Fiji software. Colour channels were split and a fixed intensity threshold was applied to the red channel. On each image, the thresholded area over the total image area was calculated. Area fractions were measured on images of at least 9 plaques and 15 plaque-free regions per animal. To exclude an influence of plaque size on microglial HIF-1α levels, plaques of similar size were selected for analysis of HIF-1α levels in the different treatment groups (average plaque size: PBS i.p.: 1.73 ± 0.15, 1 × LPS i.p.: 1.84 ± 0.19, 4 × LPS i.p. 2.27 ± 0.39% Congo red area fraction).

For nuclear HIF-1α staining, a modified staining protocol was used. In brief, sections were blocked with mouse immunoglobulin blocking reagent (Vector laboratories) for 1 h at room temperature, followed by blocking with normal donkey serum for 1 h at room temperature. Sections were then incubated overnight with mouse anti-HIF1α (clone mgc3, 1:50; Thermo Fisher Scientific, catalogue no. MA1-516) and rabbit anti-Pu.1 (1:250; New England Biolabs, catalogue no. 2258S. Clone 9G7) at 4 °C. To quantify the intensity of nuclear HIF-1α staining, z-stacks from three plaques and plaque-free regions per animal were acquired with the same microscope settings and subsequently analysed with IMARIS 8.3.1 software. Using the surfaces tool, a mask based on microglial nuclei was created using staining for Pu.1. A filter for area was applied to exclude background staining. The created surface was used to mask the HIF-1α channel. The mean masked HIF-1α intensity was then determined.

To quantify neuronal dystrophy, fluorescent images from 5–10 plaques per animal were acquired with the same microscope settings and subsequently analysed with Fiji software. Maximum intensity projections were generated to choose the region of interest consisting of APP staining and the plaque. Fluorescence channels were split, and intensity thresholds were applied to each channel. For every plaque, the thresholded area within the region of interest was calculated as a measure of plaque size and dystrophic area.

**Stereological and morphological quantification.** Stereological quantification was performed by a blinded observer on random sets of every 12th systematically sampled 25-μm thick sections throughout the neocortex. Analysis was conducted using the Stereologer software (Stereo Investigator 6; MBF Bioscience) and a motorized x–y–z stage coupled to a video microscopy system (Optronics). For quantification of total Pu.1- and GFAP-positive cells, the optical fractionator technique was used with 3D dissectors as previously described[45]. For the quantification of plaque-associated cells, plaques were identified by Congo red staining and cells in their immediate vicinity were counted. Plaque load was determined by analysing the

cortical area covered by Congo Red and/or anti-Aβ staining using the area fraction fractionator technique[45]. The volume of neuronal damage and microglial activation after brain ischaemia was determined using the Cavalieri estimator technique.

To analyse microglial morphology, we acquired three images from three non-consecutive Iba-1 immunostained brain sections per animal using identical camera acquisition settings, at 20×/0.5NA magnification. In order to perform the filament tracing in IMARIS (v.8.3.1), images were pre-processed in Fiji to optimize their contrast for reconstruction. The image background was subtracted using the inbuilt Fiji plugin to obtain an evenly distributed intensity and enhance contrast to the cells; subsequently the images were sharpened and their intensity was adjusted to the respective minimum and maximum histogram values. Filaments were then traced in IMARIS using the in-built Autopath algorithm. Reconstruction parameters were kept constant among all images; each cell was reconstructed as a 'filament' element in IMARIS, associated with a total length and volume.

**Enzyme-linked immunosorbent assay (ELISA).** For quantification of Aβ by ELISA (Meso Scale Discovery) in brain homogenates or by single molecule array (SIMOA, Quanterix) in isolated microglial cells, samples were pre-treated with formic acid (Sigma-Aldrich, final concentration: 70% vol/vol), sonicated for 35 s on ice, and centrifuged at 25,000g for 1 h at 4 °C. Neutralization buffer (1 M Tris base, 0.5 M Na$_2$HPO$_4$, 0.05% NaN$_3$ (wt/vol)) was then added at a 1:20 ratio. Aβ was measured by an observer blinded to the treatment groups using human (6E10) Aβ triplex assay (Meso Scale Discovery, MSD) in brain homogenates or Simoa Human Abeta 42 2.0 Kit (Quanterix) in isolated microglia according to the manufacturer's instructions.

Soluble APPβ containing the Swedish mutations (as present in the APP23 transgene) was measured using the sw soluble APPβkit (Mesoscale Discovery) following the manufacturer's instructions after extraction with 1% Triton X-100 and ultracentrifugation for 1 h (135,000g at 4 °C).

For cytokine measurements, brain homogenates were centrifuged at 25,000g for 30 min at 4 °C. Supernatants were analysed using the mouse pro-inflammatory panel 1 V-plex plate (Mesoscale Discovery) according to the manufacturer's instructions. To determine blood cytokines, serum was obtained by coagulation of whole blood in Vacuettes (Greiner Bio-One) for 10 min at room temperature and centrifugation for 10 min at 2,000g. Serum samples were diluted 1:2 before measurements. The investigator was blinded to the treatment groups.

Measurements were performed on a Mesoscale Sector Imager 6000 or a Simoa HD-1 Analyzer. For analyses of brain homogenates, protein levels were normalized against total protein amount as measured by BCA protein assay (Pierce).

To determine levels of LPS in blood and brain homogenates, the Limulus Amebocyte Lysate assay was used according to the manufacturer's instructions (Pierce LAL Chromogenic Endotoxin Quantitation Kit). Standards were prepared either in serum or brain homogenate from non-injected control animals. Serum samples were diluted 1:100 and brain homogenates 1:5 to eliminate matrix effects.

**Isolation of microglia and fluorescence-activated cell sorting analysis.** Fluorescence-activated cell sorting of microglia was performed on the basis of CD11b^{high} and CD45^{low} as previously described[9] (Extended Data Fig. 6).

**Assessment of microglial mitochondrial membrane potential and lactate release.** To assess the microglial mitochondrial membrane potential, 10,000 microglia were sorted into 70 µl PBS. Cells were incubated at 37 °C with 3,3′-dihexyloxacarbocyanine iodide (DiOC$_6$(3); Thermo Fisher Scientific) at a final concentration of 0.2 nM for 20 min. At this concentration, mitochondrial dye accumulation is largely dependent on the mitochondrial membrane potential, with only minor contributions of the plasma membrane potential[46]. After incubation, the cell suspension was diluted with ice-cold PBS and DiOC$_6$(3) fluorescence was immediately acquired with a Sony SH800 instrument.

For the assessment of microglial lactate release, 50,000 microglia from the same animals as used for DiOC$_6$(3) staining were plated in 96-well plates with 125 µl macrophage serum-free medium (Thermo Fisher Scientific) and incubated for 24 h at 37 °C with 5% CO$_2$. Lactate concentration in the medium was determined using a Lactate Assay Kit (BioVision) following the manufacturer's instructions and was correlated to DiOC$_6$(3) fluorescence values from cells of the same animal using IBM SPSS Statistics 22 software.

**RNA sequencing.** For RNA sequencing, 10,000 microglia were directly sorted into RNase-free PCR strips containing 30 µl H$_2$O with 0.2% Triton X-100 and 0.8 U/µl RNase inhibitor (Clontech) and samples were immediately frozen on dry ice. RNA was isolated using NucleoSpin RNA XS kit (Macherey-Nagel) according to the manufacturer's instructions. Three nanograms total RNA was used as input material for cDNA synthesis. cDNA synthesis and enrichment were performed following the Smart-seq2 v4 protocol as described by the manufacturer (Clontech). Sequencing Libraries were prepared with 1 ng of cDNA using the Nextera XT library preparation kit (Illumina) as described[47]. Multiplexing of samples was achieved using three different index-primers in each lane. For sequencing, samples from each group (APP and wild-type) were pooled to rule out amplification and sequencing biases. Libraries were quality-controlled and quantified using a

Qubit 2.0 Fluorometer (Life Technologies) and Agilent 2100 Bioanalyzer (Agilent Technologies). A final library concentration of 2 nM was used for sequencing. Sequencing was performed using a 50-bp single read setup on the Illumina HiSeq 2000 platform.

Base calling from raw images and file conversion to fastq files were achieved by Illumina standard pipeline scripts (bcl2fastq v.2.18.0). Quality control was then performed using FASTQC (v.2.18.0) program (http://www.bioinformatics. babraham.ac.uk/projects/fastqc/), eliminating one sample that had fewer than 20 million reads. Reads were trimmed off for sequencing adaptor and were mapped to mouse reference transcriptome (mm10) using STAR aligner 2.5.2b with non-default parameters. Unique read counts were obtained for each sample using HOMER v.4.8 software (http://homer.salk.edu/homer/) and the 'maketagdirectory -tbp 1' command, followed by 'analyzeRepeats.pl rna mm10 -count exons -noadj -condenseGenes'. Raw read counts were imported into R (v.3.2) and normalized using the Bioconductor (v.3.2) DESeq2 package (v.1.10.1) using default parameters. After normalization, all transcripts with a maximum overall group mean lower than 10 were removed. Unwanted or hidden sources of variation, such as batch and preparation date, were removed using the sva package[48]. The normalized rlog transformed expression values were adjusted according to the surrogate variables identified by sva using the function removeBatchEffect from the limma package[49]. To determine gene clusters associated with wild-type or APP23 animals following i.p. injections (1 × LPS or 4 × LPS) at 3 months of age, we then used the 13,627 present genes and applied the R implementation of WGCNA. We then performed WGCNA clustering using the '1-TOMsimilarityFromExpr' function with the network type 'signed hybrid', a power parameter of 7 (as established by scale-free topology network criteria), and a minimum module size of 50, dissecting the data into 10 modules. Finally, pathway enrichment analysis of genes within modules was performed using the 'findmotifs.pl' function of HOMER. Correction for multiple comparisons for KEGG pathway analyses was performed using the STATS package of R and applying the Benjamini–Hochberg correction. To focus on the most important molecular pathways, only pathways with logP ≤ −3 and at least five genes were considered.

**Chromatin immunoprecipitation, library preparation and analysis.** To isolate microglia for chromatin purification, 1 mM sodium butyrate, an inhibitor of histone deacetylases[30], was added to the dissection medium and FACS buffers. After staining, microglia were fixed in 1% PFA for 10 min at room temperature, followed by addition of glycine (final concentration: 125 mM) for 5 min and washing in HBSS. Microglia were then sorted into homogenization buffer (0.32 M sucrose, 5 mM CaCl$_2$, 5 mM magnesium acetate, 50 mM HEPES, 0.1 mM EDTA, 1 mM DTT, 0.1% vol/vol Triton X-100) and centrifuged at 950g for 5 min at 4 °C. The pellet was resuspended in 100 µl Nelson buffer (50 mM Tris, 150 mM NaCl, 20 mM EDTA, 1% vol/vol Triton X-100, 0.5% vol/vol NP-40) and frozen on dry ice.

Chromatin immunoprecipitation with sequencing (ChIP–seq) was performed as previously described[50], with slight modifications. In brief, two biological replicates were analysed for each condition and targeted histone modification. Cell lysates from 8–10 mice were pooled, giving a total cell number of approximately 0.8 million to 1 million cells per replicate. The cross-linked chromatin was sheared for 3 × 7 cycles (30 s on/off) in a BioruptorPlus (Diagenode) to achieve an average fragment size of 350 bp. Proper shearing and chromatin concentration were validated by DNA isolation and quantification using a small amount of each sample individually. Samples were split in half and 1 µg of ChIP-grade antibody (H3K4me1: Abcam ab8895 or H3K27ac: Abcam ab4729) was added and incubated overnight at 4 °C. From each sample, 1% of the total volume was taken as input control before antibody binding. Immunoprecipitation was performed by incubating samples with 30 µl BSA-blocked protein A magnetic beads (Dynabeads, Invitrogen) for 1 h at 4 °C. After purifying the precipitated chromatin and isolating the DNA, DNA libraries were generated using the Next Ultra DNA Library Prep Kit for Illumina and the Q5 polymerase (New England Biolabs). Multiplexing of samples was done using six different index primers from the Library Prep Kit. For each replicate, samples from each condition (genotype and treatment) were pooled to rule out amplification and sequencing biases within the final data. Input samples were pooled and processed accordingly. The ideal number of amplification cycles was estimated via RealTime PCR to avoid over-amplification. Accordingly, samples were amplified for 13–15 cycles and the DNA was isolated afterwards. Individual libraries were pooled; each pool represented one whole batch of samples for each condition and targeted histone modification and was set to a final DNA concentration of 2 nM before sequencing (50 bp) on a HiSeq 2000 (Illumina) according to the manufacturer's instructions.

Base calling from raw images and file conversion to fastq files were achieved using standard Illumina pipeline scripts. Sequencing reads were then mapped to the mouse reference genome (mm10) using rna-STAR aligner v2.3.0 with non-default parameters. Data were further processed using HOMER software (http:// homer.salk.edu/homer/), following two recently published analyses on micro-glial epigenetic profiles[30,31]. Tag directories were created from bam files using

'makeTagDirectory' for individual samples and inputs, and peak calling was performed using 'findpeaks -style histone' with fourfold enrichment over background and input, a Poisson *P* value of 0.0001, and a peak width of 500 bp for H3K4me1 and 250 bp for H3K27ac. Peaks common to both replicates were determined using 'mergepeaks' (-prefix) function. To focus analysis on enhancers, peaks within ± 2.5 kb of known transcription start sites were filtered out. Union peak files for H3K4me1 and H3K27ac marks were then created for group-wise comparisons using 'mergepeaks' function. Active enhancers, that is, genomic regions containing both H3K4me1 and H3K27ac peaks, were identified using the 'window' function of bedtools2[51], requiring peaks of both marks to be located within a genomic region of 4 kb. Union peak files of active enhancers were then used for comparisons amongst groups for both H3K4me1 and H3K27ac marks using the 'getDifferentialPeaks' function (using a fold-change cut-off of 1.5 and a cumulative Poisson *P* value of 0.0001). Finally, differential peaks were annotated using the 'annotatepeaks.pl' function, including gene ontology analysis. Correction for multiple comparisons for KEGG pathway analyses was performed using the STATS package of R and applying the Benjamini–Hochberg correction. To focus on the most important molecular pathways, only pathways with $\log P \leq -3$ and at least three genes were considered.

For the generation of UCSC browser files, the 'makeUCSCfile' function was used, including normalization to respective input and library size, with a resolution of 10 bp. Files for heatmaps of 24 kb genomic regions and with a resolution of 250 bp were generated using the 'annotatePeaks.pl' function; clustering was then performed using Gene Cluster 3.0 and visualized using JavaTreeView 1.16r4.

To identify transcription factors involved in the differential activation of enhancers, the 'findMotifsGenome.pl' command was used to analyse a region of 500 bp around enhancer peaks ('-size 500'), as this resulted in more robust identification of motifs for known microglial lineage-determining transcription factors when determining motifs of all identified microglial enhancers (Extended Data Fig. 8). For all active enhancers, motif analysis was performed using the union H3K27ac peak file and standard background (that is, random genomic sequence created by HOMER). In the case of pairwise comparisons amongst conditions, the first condition's specific H3K27ac peak file was used as input and the second condition's peak file as background. Because motif enrichment was often relatively low, we focused on the most relevant results by determining transcription factor (families), whose motifs occurred at least twice in 'known' and 'de-novo' motifs.

**Comparison between enhancer activation and gene expression.** From our 14 pairwise comparisons (Fig. 4, Extended Data Fig. 7 and Supplementary Table 2), we analysed 772 differentially activated enhancers and compared increased or decreased H3K27ac levels with the direction of change in the expression of the nearest gene (difference in *z*-scores between the groups used for pairwise comparisons). The 14 concordance values were then statistically compared to chance level (50%) using a two-tailed Wilcoxon signed rank test.

**Reporting summary.** Further information on experimental design is available in the Nature Research Reporting Summary linked to this paper.

**Statistics and reproducibility.** Statistical analyses were performed using IBM SPSS Statistics 22 or Prism 5 software. Data were assessed for normal distribution (Shapiro–Wilk test) and statistical outliers using the 'explore' function. If the normality criterion was met, data were analysed using a one-way ANOVA (for experiments on single genotypes), followed by pairwise comparison (if $P < 0.05$) with post-hoc Tukey correction (for samples with non-significant homogeneity of variance Levene's test) or Dunnett test (if homogeneity of variances not given). For comparisons across treatments and genotypes (for example, cytokine analyses in Fig. 2), a two-way ANOVA was performed, followed by post-hoc testing with Tukey correction for significant main effects ($P < 0.05$). As the cytokine data for acute LPS stimulation (Fig. 1) showed inequality of variance as well as skewedness, a non-parametric independent-samples median test was performed followed by pairwise comparison with correction for multiple comparison.

All experiments were performed at least twice and in independent batches of animals for key findings (figures show the pooled data). Owing to batch-related variation in some dependent variables, 'batch' was added as a random variable to analyses where a significant batch effect was observed. For datasets with small sample size (for example, western blotting analyses), the Kruskal–Wallis test was performed, followed by pairwise comparisons if $P < 0.05$. In the figure legends, *n* denotes the number of animals per treatment group. Minimum sample sizes were determined a priori using power analyses or as dictated by the methodology (for example, ChIP–seq).

Raw and processed data are provided in the Gene Expression Omnibus (accession number GSE82170; subseries GSE82168 for ChIP–seq and GSE104630 for RNA-seq datasets). Other data that support the findings of this study are available from the corresponding author upon reasonable request.

40. Liu, F., Yuan, R., Benashski, S. E. & McCullough, L. D. Changes in experimental stroke outcome across the life span. *J. Cereb. Blood Flow Metab.* **29**, 792–802 (2009).
41. Sturchler-Pierrat, C. & Staufenbiel, M. Pathogenic mechanisms of Alzheimer's disease analyzed in the APP23 transgenic mouse model. *Ann. NY Acad. Sci* **920**, 134–139 (2000).
42. Neher, J. J. et al. Phagocytosis executes delayed neuronal death after focal brain ischemia. *Proc. Natl Acad. Sci. USA* **110**, E4098–E4107 (2013).
43. Hefendehl, J. K. et al. Repeatable target localization for long-term *in vivo* imaging of mice with 2-photon microscopy. *J. Neurosci. Methods* **205**, 357–363 (2012).
44. Eisele, Y. S. et al. Peripherally applied Aβ-containing inoculates induce cerebral β-amyloidosis. *Science* **330**, 980–982 (2010).
45. Varvel, N. H. et al. Replacement of brain-resident myeloid cells does not alter cerebral amyloid-β deposition in mouse models of Alzheimer's disease. *J. Exp. Med.* **212**, 1803–1809 (2015).
46. Rottenberg, H. & Wu, S. Quantitative assay by flow cytometry of the mitochondrial membrane potential in intact cells. *Biochim. Biophys. Acta* **1404**, 393–404 (1998).
47. Picelli, S. et al. Full-length RNA-seq from single cells using Smart-seq2. *Nat. Protocols* **9**, 171–181 (2014).
48. Leek, J. T., Johnson, W. E., Parker, H. S., Jaffe, A. E. & Storey, J. D. The sva package for removing batch effects and other unwanted variation in high-throughput experiments. *Bioinformatics* **28**, 882–883 (2012).
49. Ritchie, M. E. et al. limma powers differential expression analyses for RNA-sequencing and microarray studies. *Nucleic Acids Res.* **43**, e47 (2015).
50. Halder, R. et al. DNA methylation changes in plasticity genes accompany the formation and maintenance of memory. *Nat. Neurosci.* **19**, 102–110 (2016).
51. Quinlan, A. R. BEDTools: The Swiss-army tool for genome feature analysis. *Curr. Protoc. Bioinformatics* **47**, 11.12.1–11.12.34 (2014).
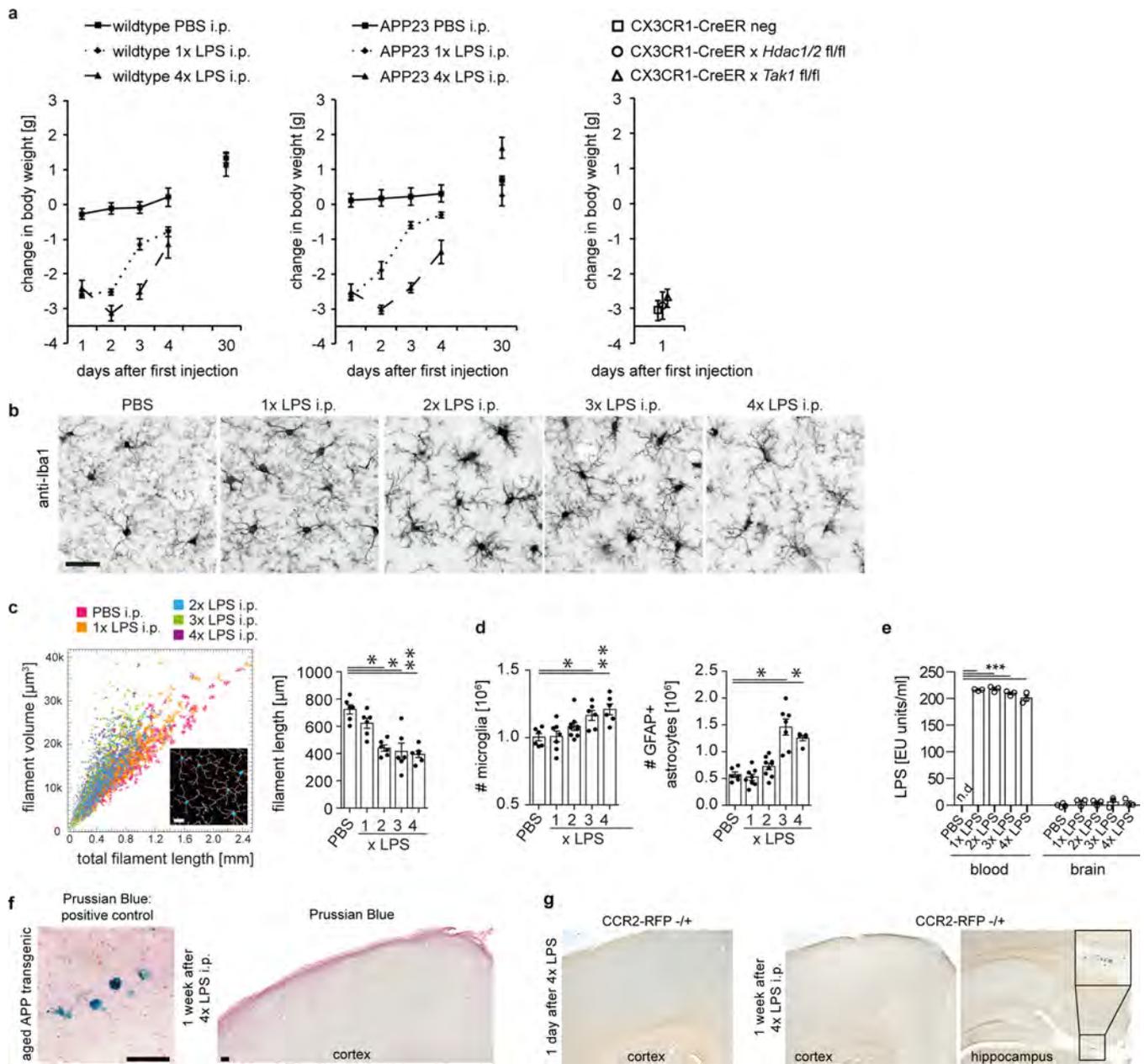
**Extended Data Fig. 1 | Acute responses to LPS injections. a**, Weight changes after injection of LPS (wild-type mice: $n = 11, 11, 11, 11, 4$ from left to right for PBS, $n = 9, 9, 9, 8, 7$ for $1 \times$ LPS, $n = 10, 10, 10, 10, 7$ for $4 \times$ LPS; APP animals: $n = 14, 14, 14, 14, 7$ for PBS, $n = 8, 8, 8, 5, 5$ for $1 \times$ LPS; $n = 10, 10, 10, 10, 10$ for $4 \times$ LPS; Cre mice: $n = 5, 5, 4$). **b**, **c**, Morphological changes in microglia ($n = 6, 6, 6, 6, 6$ mice). Scale bar, 50 μm. **d**, Numbers of microglia and activated (GFAP$^+$) astrocytes (microglia: $n = 6, 7, 8, 6, 6$ mice, astrocytes: $n = 6, 8, 9, 7, 5$ mice). **e**, Blood and brain levels of LPS after daily injections with 500 μg per kg bodyweight ($n = 4, 3, 3, 3, 3$ animals). **f**, Assessment of iron entry from the blood (detected by Prussian blue staining) shows positive staining in an aged (>25 months) APP transgenic mouse, but not after repeated intraperitoneal LPS injections ($n = 3$ mice analysed). **g**, In heterozygous mice expressing red fluorescent protein (RFP) under the type 2 CC chemokine receptor (Ccr2) promoter, no entry of CCR2-expressing blood monocytes was detected after repeated LPS injection (staining for RFP; insert shows RFP-positive monocytes in the choroid plexus; $n = 3$ mice analysed). Scale bar, 100 μm. Data are means ± s.e.m. *$P < 0.05$, **$P < 0.01$, ***$P < 0.001$ for one-way ANOVA with Tukey correction.
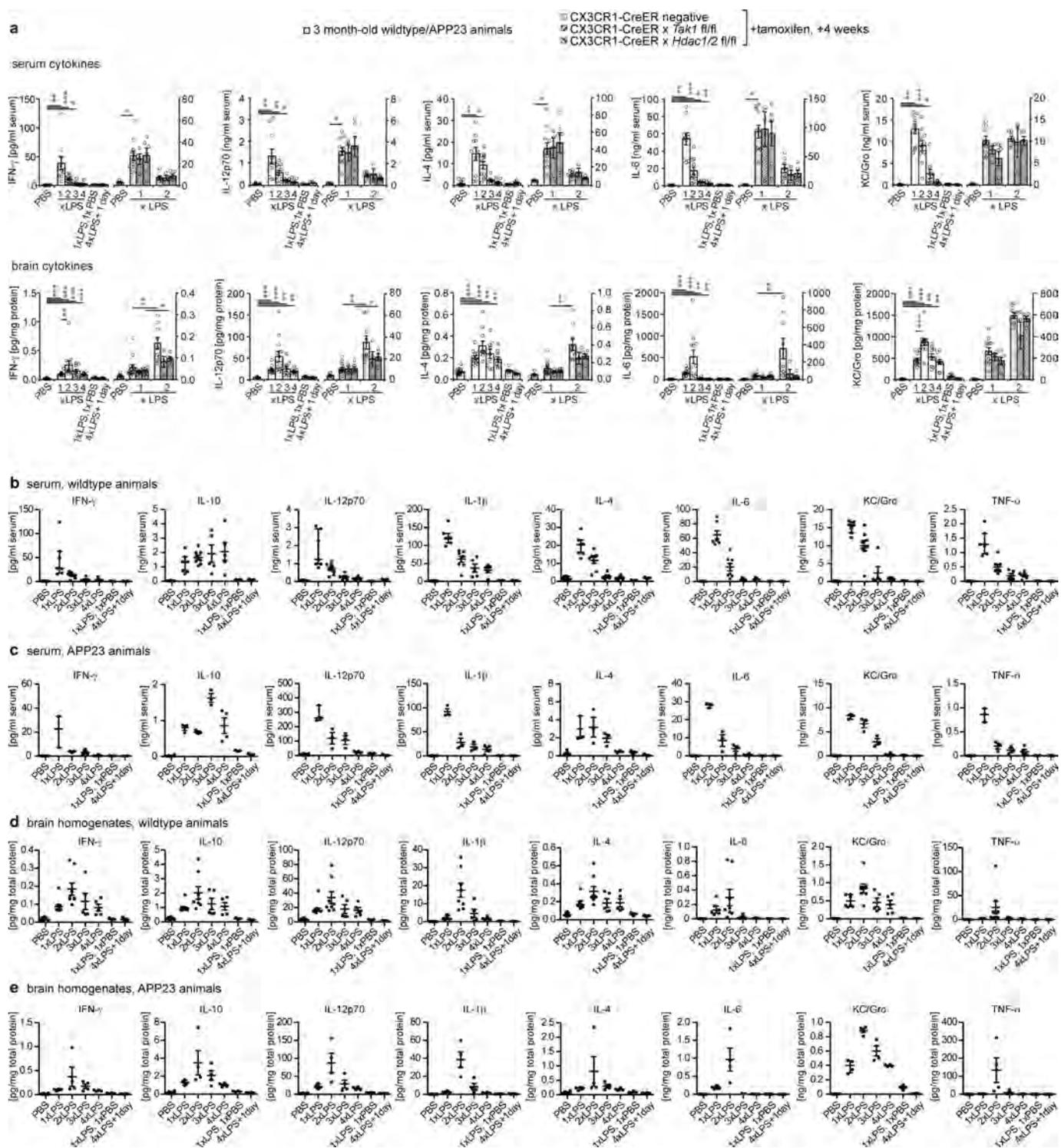
**Extended Data Fig. 2 | Cytokine response after acute LPS injections.** **a**, Additional cytokines (Fig. 1) analysed in the serum (top) and brain (bottom) 3 h after each daily intraperitoneal LPS injection on four consecutive days in 3-month-old mice (control mice received PBS injections; $n = 16, 11, 12, 9, 9, 7, 7$ and $5, 13, 4, 6, 9, 9, 4, 5$ mice for groups from left to right). **b**, **c**, Cytokine response in the blood only in wild-type (**b**, $n = 6, 7, 8, 5, 5, 3, 3$ mice) or APP23 mice (**c**, $n = 10, 3, 3, 3, 4, 3, 3$ mice). **d**, **e**, Cytokine response in the brain only in wild-type (**d**, $n = 6, 7, 8, 5, 5, 3, 3$ mice) or APP23 mice (**e**, $n = 10, 4, 4, 4, 4, 4, 4$ mice). Data are means ± s.e.m. $*P < 0.05$, $**P < 0.01$, $***P < 0.001$ for independent-samples median test with correction for multiple comparisons.
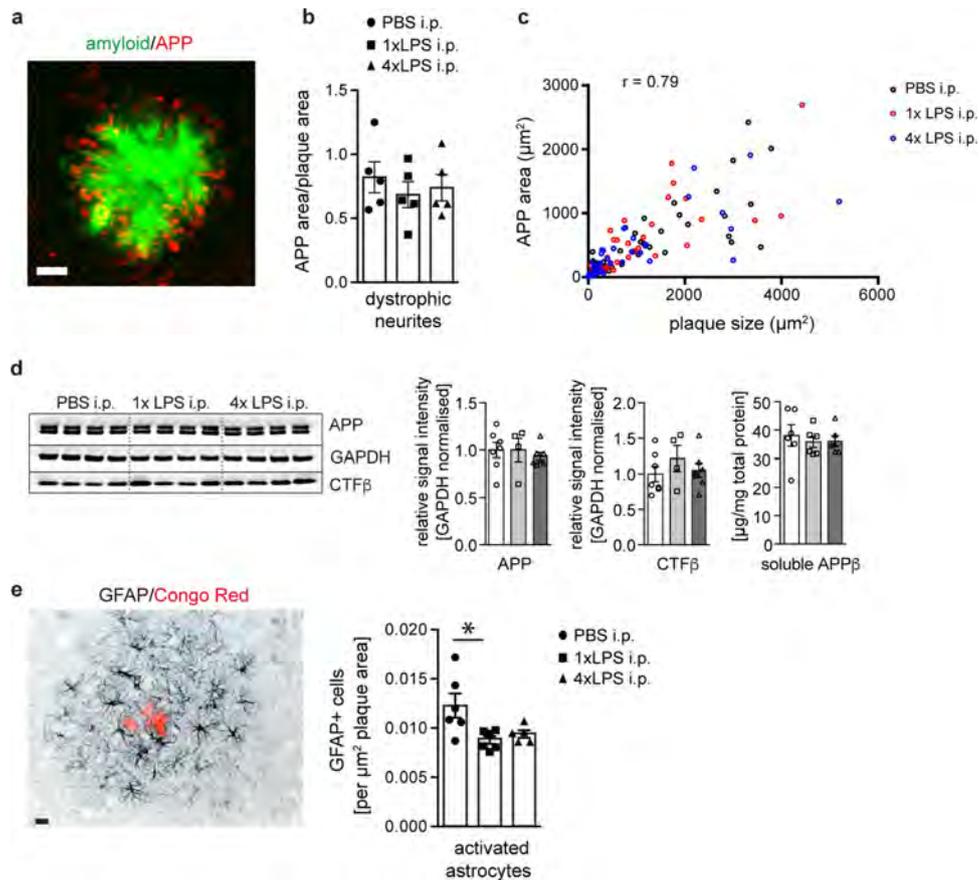
**Extended Data Fig. 3 | APP levels and processing, neuritic dystrophy and astrocyte activation in 9-month-old APP23 animals.**
**a**, **b**, Micrograph of fluorescent staining for amyloid plaque (Methoxy-X04; green) and amyloid precursor protein (APP; red) (**a**) shows neuritic dystrophy surrounding the amyloid deposit, which is unchanged by LPS treatments (**b**; $n = 5, 5, 5$ animals). **c**, Overall Pearson's correlation of plaque size with neuritic dystrophy (APP area; $n = 49, 39, 42$ plaques for PBS, $1 \times$ LPS, $4 \times$ LPS groups). **d**, Western blotting analysis (for gel source data, see Supplementary Fig. 1) of brain homogenates for APP and C-terminal fragment-$\beta$ (CTF$\beta$; $n = 7, 4, 7$ mice), and soluble APP$\beta$ ELISA ($n = 6, 6, 6$ mice). **e**, Micrograph of activated astrocytes (glial fibrillar acidic protein: GFAP) surrounding an amyloid plaque (Congo red) and quantification of the number of plaque-associated GFAP-positive astrocytes ($n = 6, 6, 5$ mice). Scale bar, 10 μm (**a**), 20 μm (**e**). Data are means ± s.e.m. *$P < 0.05$ for one-way ANOVA with Tukey correction.
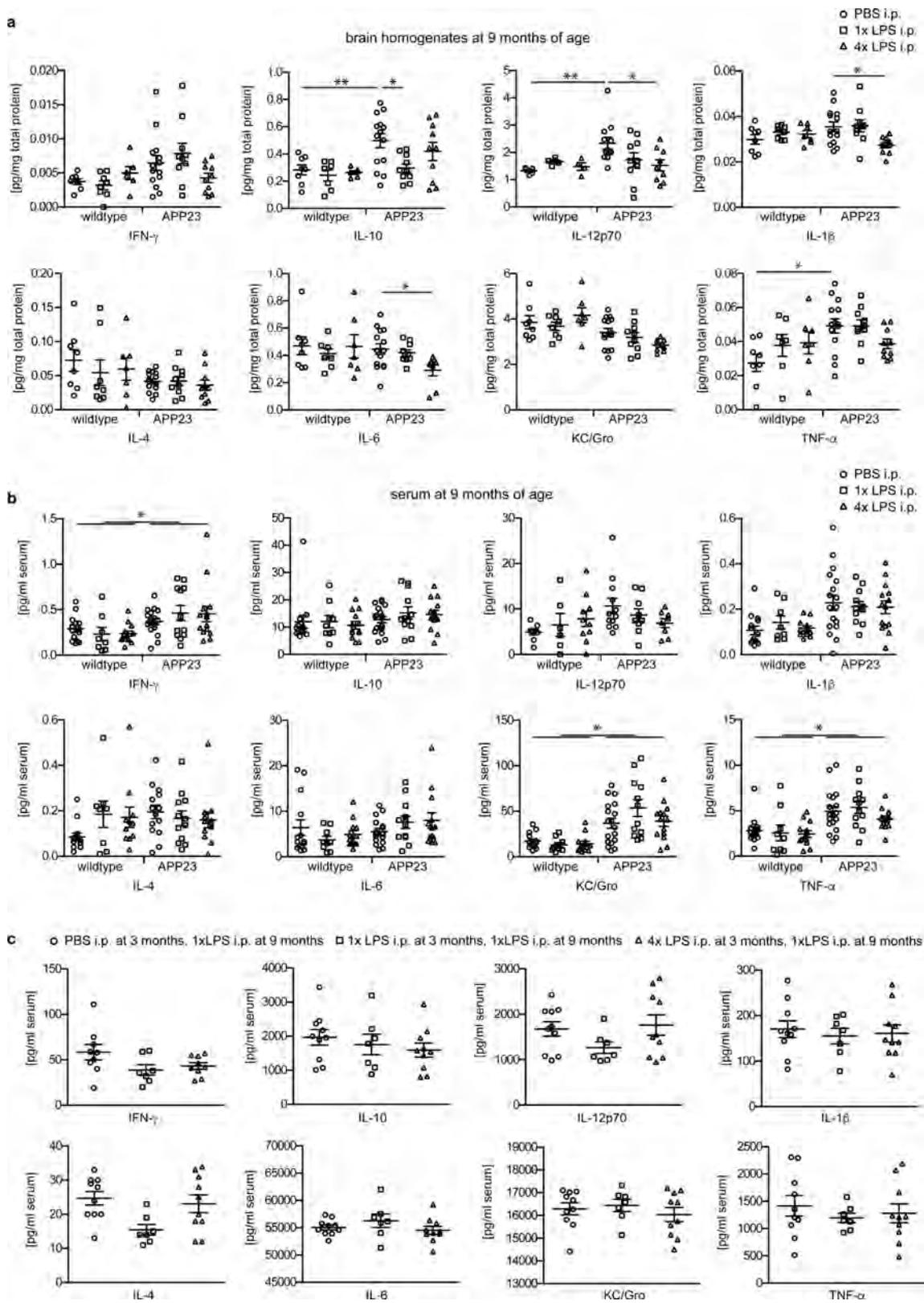
**Extended Data Fig. 4 | Cytokine levels in 9-month-old animals.**
**a**, Cytokine measurements in brain homogenates of 9-month-old wild-type ($n = 8, 8, 7$ mice) and APP23 mice ($n = 14, 10, 10$ mice) treated i.p. with $1 \times$ LPS or $4 \times$ LPS at 3 months of age. **b**, Cytokine measurements in the serum of 9-month-old wild-type (WT; $n = 14, 9, 13$ mice) and APP23 mice (APP; $n = 18, 12, 14$ mice) after i.p. stimulation with $1 \times$ LPS or $4 \times$ LPS at 3 months of age. **c**, Cytokine measurements in the serum of

wild-type mice stimulated i.p. with $1 \times$ LPS or $4 \times$ LPS at 3 months of age and re-stimulated with an additional LPS injection ($500\,\mu g\,kg^{-1}$) at 9 months of age ($n = 10, 7, 10$ animals). Data are means $\pm$ s.e.m. *$P < 0.05$, **$P < 0.01$ for two-way ANOVA with Tukey correction. In **b** a significant main effect for genotype is indicated by bars spanning all conditions of the same genotype.
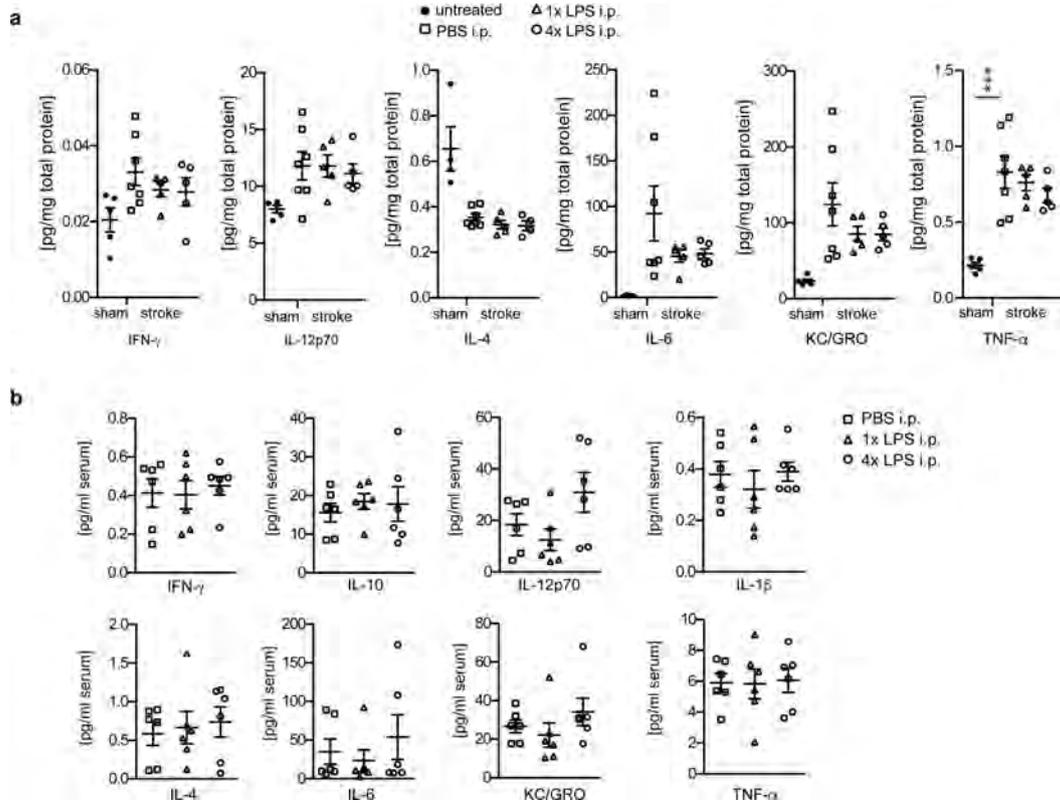
**Extended Data Fig. 5 | Cytokine levels after brain ischaemia and in blood of 4-month-old mice.** Three-month-old animals were injected i.p. with $1 \times$ LPS or $4 \times$ LPS and incubated for 4 weeks before receiving a stroke. **a**, Cytokine measurements in brain homogenates 24 h after stroke ($n = 5, 7, 5, 5$ animals). **b**, Cytokine measurements in the serum ($n = 6, 6, 6$ animals). Data are means $\pm$ s.e.m. ***$P < 0.001$ for one-way ANOVA with Tukey correction.
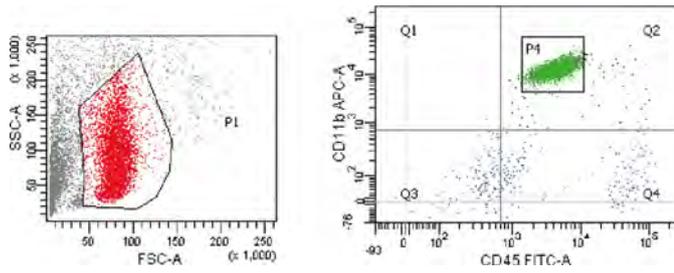
**Extended Data Fig. 6 | Microglial sorting strategy.** Microglia were sorted as CD11b$^{high}$ and CD45$^{low}$ cells (population P4) from 9-month-old APP23 mice or wild-type littermates following i.p. injections of $1 \times$ LPS or $4 \times$ LPS at 3 months of age.
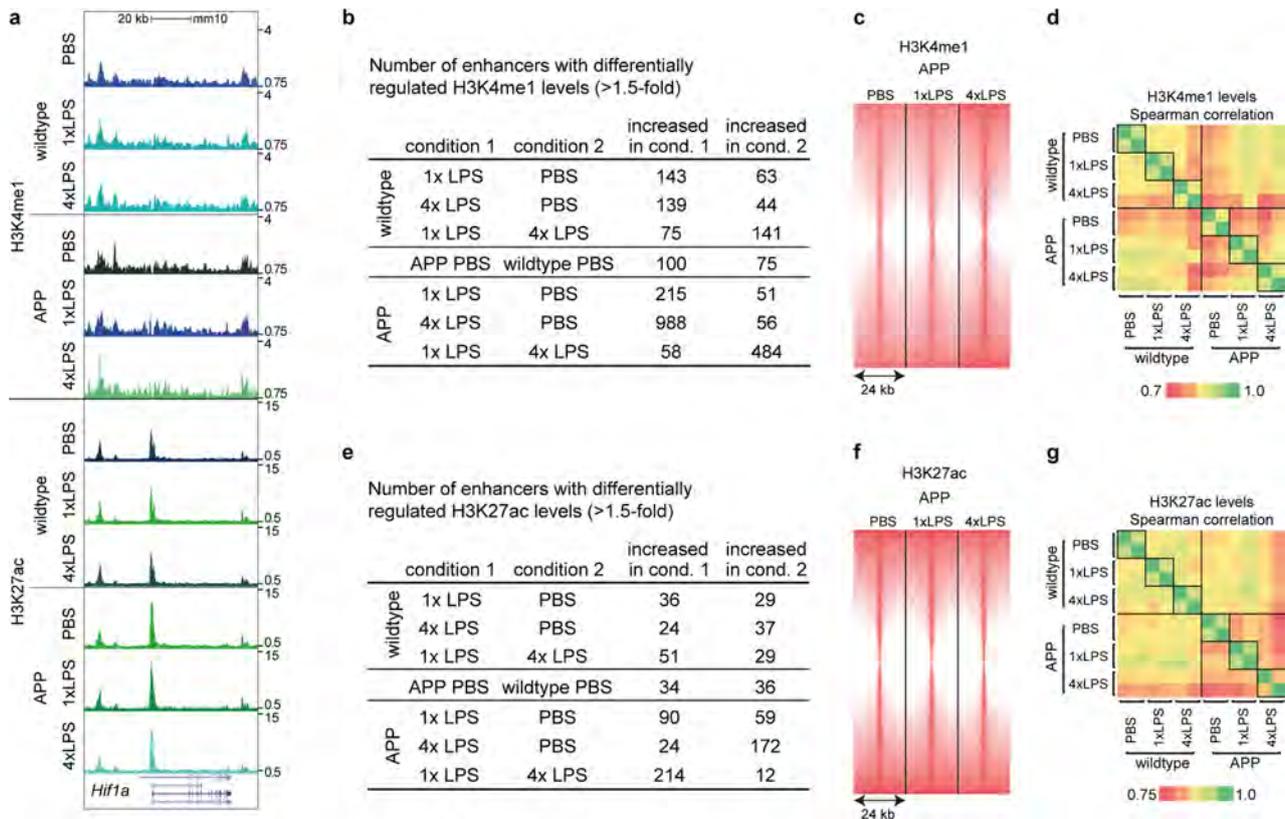
**Extended Data Fig. 7 | Analysis of microglial enhancers.** Microglial enhancers were analysed in 9-month-old wild-type and APP23 (APP) mice treated intraperitoneally with 1 × LPS or 4 × LPS at 3 months of age. **a**, Exemplary UCSC browser images of genomic region around the *Hif1a* gene (normalized to input and library dimension). **b**, Numbers of regions with differentially regulated H3K4me1 levels. **c**, Heatmaps of H3K4me1 regions (centred on H3K27ac peaks). **d**, Pairwise correlations between the two replicates of H3K4me1 read densities in differentially regulated regions. **e–g**, Analyses of H3K27ac levels analogous to **b–d** for H3K4me1. $n = 2$ replicates (8–10 mice per replicate); differential enhancers showed a cumulative Poisson $P < 0.0001$.

**a** — motifs enriched in all active enhancers (random background):

| Known motifs Best Match | P-value | Targets | Background |
|---|---|---|---|
| PU.1(ETS) | 1e-624 | 26.58% | 12.58% |
| ELF5(ETS) | 1e-549 | 32.44% | 17.80% |
| SpiB(ETS) | 1e-511 | 14.65% | 5.42% |
| ETS1(ETS) | 1e-492 | 39.47% | 24.34% |
| ETV1(ETS) | 1e-471 | 47.55% | 31.83% |

| De novo motifs Best Match | P-value | Targets | Background |
|---|---|---|---|
| Sfpi1 | 1e-946 | 39.65% | 19.51% |
| PU.1:IRF8 | 1e-101 | 48.30% | 40.82% |
| Mef2a | 1e-91 | 10.79% | 6.90% |
| RUNX2 | 1e-78 | 41.54% | 35.16% |
| Foxo1 | 1e-70 | 29.13% | 23.68% |

**b** — comparison: known and de novo motifs enriched in enhancers of condition 1 and condition 2

**Condition 1: APP PBS — Condition 2: wildtype PBS**

Condition 1:

| Best match | P-value | Targets | Background |
|---|---|---|---|
| TCF3 | 1e-06 | 6.80% | 5.86% |
| TCF3 | 1e-36 | 0.58% | 0.10% |
| SREBP1a | 1e-03 | 4.69% | 4.16% |
| SREBP1a | 1e-34 | 0.33% | 0.04% |
| IRF4 | 1e-03 | 11.90% | 10.96% |
| IRF4 | 1e-25 | 0.27% | 0.04% |
| Mef2c | 1e-03 | 12.17% | 11.31% |
| Mef2b | 1e-57 | 0.53% | 0.05% |

Condition 2:

| Best match | P-value | Targets | Background |
|---|---|---|---|
| TGIF2 | 1e-14 | 69.21% | 65.97% |
| TGIF1 | 1e-08 | 66.14% | 63.66% |
| TGIF2 | 1e-40 | 0.30% | 0.01% |
| IRF4 | 1e-50 | 0.50% | 0.04% |
| IRF4 | 1e-23 | 0.26% | 0.03% |
| Smad2/3 | 1e-29 | 1.03% | 0.32% |
| Smad3 | 1e-26 | 0.28% | 0.03% |
| Smad2 | 1e-19 | 1.77% | 0.92% |
| ATF1 | 1e-26 | 0.28% | 0.03% |
| ATF1 | 1e-25 | 0.27% | 0.03% |

**Condition 1: APP 1xLPS — Condition 2: APP 4xLPS**

Condition 1:

| Best match | P-value | Targets | Background |
|---|---|---|---|
| CEBPb | 1e-08 | 13.68% | 12.23% |
| CEBPb | 1e-02 | 16.62% | 15.82% |
| GATA2 | 1e-06 | 15.98% | 14.62% |
| GATA1 | 1e-05 | 14.26% | 13.10% |
| GATA4 | 1e-04 | 24.00% | 22.65% |
| GATA3 | 1e-04 | 34.99% | 33.52% |
| GATA4 | 1e-43 | 0.32% | 0.03% |
| HIF-1b | 1e-05 | 22.67% | 21.23% |
| HIF-1a | 1e-02 | 4.20% | 3.77% |
| HIF-1a | 1e-24 | 0.69% | 0.23% |
| ARNT:HIF1A | 1e-17 | 0.27% | 0.06% |
| AP-2gamma | 1e-04 | 22.16% | 20.85% |
| AP-2alpha | 1e-03 | 16.77% | 15.77% |
| MYB | 1e-04 | 39.46% | 38.06% |
| MYB | 1e-53 | 0.56% | 0.07% |
| MYB | 1e-53 | 0.30% | 0.01% |
| TEAD4 | 1e-04 | 18.79% | 17.65% |
| TEAD4 | 1e-58 | 0.40% | 0.03% |
| TCFL2 | 1e-03 | 2.39% | 1.98% |
| TCFL2 | 1e-41 | 0.44% | 0.06% |
| Smad4 | 1e-02 | 42.15% | 41.21% |
| Smad4 | 1e-36 | 0.54% | 0.10% |

Condition 2:

| Best match | P-value | Targets | Background |
|---|---|---|---|
| PU.1(ETS) | 1e-10 | 24.57% | 22.45% |
| PU.1:IRF8 | 1e-04 | 8.96% | 8.11% |
| PU.1-IRF | 1e-03 | 38.94% | 37.61% |
| PU.1(ETS) | 1e-17 | 0.37% | 0.10% |
| MafK | 1e-04 | 7.18% | 6.42% |
| MafF | 1e-02 | 6.29% | 5.77% |
| MafA | 1e-02 | 22.71% | 21.88% |
| MafB | 1e-52 | 0.30% | 0.02% |
| MafA | 1e-31 | 0.26% | 0.03% |
| IRF4 | 1e-03 | 11.89% | 11.04% |
| IRF4 | 1e-45 | 0.27% | 0.02% |
| TGIF2 | 1e-02 | 67.78% | 66.88% |
| TGIF1 | 1e-02 | 64.71% | 63.81% |
| E2F | 1e-02 | 6.96% | 6.39% |
| E2F | 1e-02 | 1.93% | 1.65% |
| c-Jun | 1e-02 | 6.18% | 5.71% |
| JunD | 1e-02 | 1.85% | 1.59% |

**Condition 1: APP 1xLPS — Condition 2: APP PBS**

Condition 1:

| Best match | P-value | Targets | Background |
|---|---|---|---|
| HIF-1b | 1e-14 | 22.67% | 20.26% |
| HIF-1a | 1e-03 | 4.20% | 3.67% |
| HIF-1a | 1e-18 | 0.28% | 0.07% |
| RAR:RXR | 1e-05 | 5.71% | 4.97% |
| RARg | 1e-04 | 3.02% | 2.51% |
| GATA4 | 1e-04 | 24.00% | 22.76% |
| GATA2 | 1e-03 | 15.98% | 15.04% |
| GATA3 | 1e-03 | 34.99% | 33.77% |
| GATA1 | 1e-02 | 14.26% | 13.45% |
| MYC | 1e-59 | 0.35% | 0.01% |
| MYC | 1e-33 | 1.28% | 0.50% |
| MYC | 1e-29 | 0.27% | 0.04% |

Condition 2:

| Best match | P-value | Targets | Background |
|---|---|---|---|
| Atf4 | 1e-04 | 5.60% | 4.89% |
| Atf1 | 1e-47 | 0.43% | 0.04% |
| MafK | 1e-04 | 7.55% | 6.76% |
| MafA | 1e-03 | 23.32% | 22.13% |
| MafF | 1e-02 | 6.49% | 5.92% |
| PU.1(ETS) | 1e-02 | 23.81% | 22.80% |
| PU.1:IRF8 | 1e-02 | 8.85% | 8.27% |
| PU.1-IRF | 1e-02 | 39.43% | 38.50% |
| GATA3 | 1e-02 | 2.99% | 2.67% |
| GATA1 | 1e-51 | 0.40% | 0.02% |
| GATA3 | 1e-17 | 1.95% | 1.12% |

**Condition 1: APP 4xLPS — Condition 2: APP PBS**

Condition 1:

| Best match | P-value | Targets | Background |
|---|---|---|---|
| SpiB | 1e-15 | 13.15% | 11.19% |
| SpiB | 1e-29 | 0.31% | 0.04% |
| ATF3 | 1e-04 | 15.98% | 14.83% |
| ATF7 | 1e-02 | 9.72% | 9.05% |
| ATF1 | 1e-02 | 13.83% | 13.05% |
| JunD | 1e-04 | 1.85% | 1.47% |
| c-Jun | 1e-02 | 6.39% | 5.92% |
| MEIS1 | 1e-02 | 42.34% | 41.46% |
| MEIS1 | 1e-43 | 0.34% | 0.04% |

Condition 2:

| Best match | P-value | Targets | Background |
|---|---|---|---|
| AP-2gamma | 1e-06 | 22.50% | 20.82% |
| AP-2alpha | 1e-05 | 17.06% | 15.76% |
| Atf4 | 1e-05 | 5.60% | 4.80% |
| Atf4 | 1e-17 | 0.34% | 0.08% |
| Mef2c | 1e-05 | 12.17% | 11.05% |
| Mef2a | 1e-02 | 10.90% | 10.14% |
| Tcf4 | 1e-04 | 11.57% | 10.53% |
| Tcf4 | 1e-61 | 0.45% | 0.03% |
| Tcf3 | 1e-37 | 0.76% | 0.17% |
| CEBPb | 1e-03 | 13.80% | 12.81% |
| CEBPg | 1e-13 | 0.16% | 0.02% |
| Myb | 1e-02 | 39.82% | 38.67% |
| Myb | 1e-68 | 0.39% | 0.01% |
| Gata5 | 1e-97 | 0.51% | 0.02% |
| Gata6 | 1e-45 | 0.36% | 0.02% |
| Smad3 | 1e-27 | 6.22% | 4.28% |
| Smad2 | 1e-16 | 2.08% | 1.25% |

**Extended Data Fig. 8 | Transcription factor motif analysis of active enhancer regions.** Motif analysis was performed for selected conditions to identify transcription factors involved in the differential activation of enhancers (using putative enhancer regions present in both replicates within 500 bp around enhancer peaks). **a,** For all active enhancers, motif analysis was performed using the union H3K27ac peak file and standard background (random genomic sequence). **b,** Pairwise comparisons between conditions, using the first condition's H3K27ac peak file as input and the second condition's peak file as background. As motif enrichment was often relatively low, the analysis was focused on transcription factor (families), whose motifs occurred at least twice in 'known' (black) and 'de novo' motifs (blue). Motifs are identified by HOMER software using hypergeometric testing (no adjustment for multiple comparisons was made).
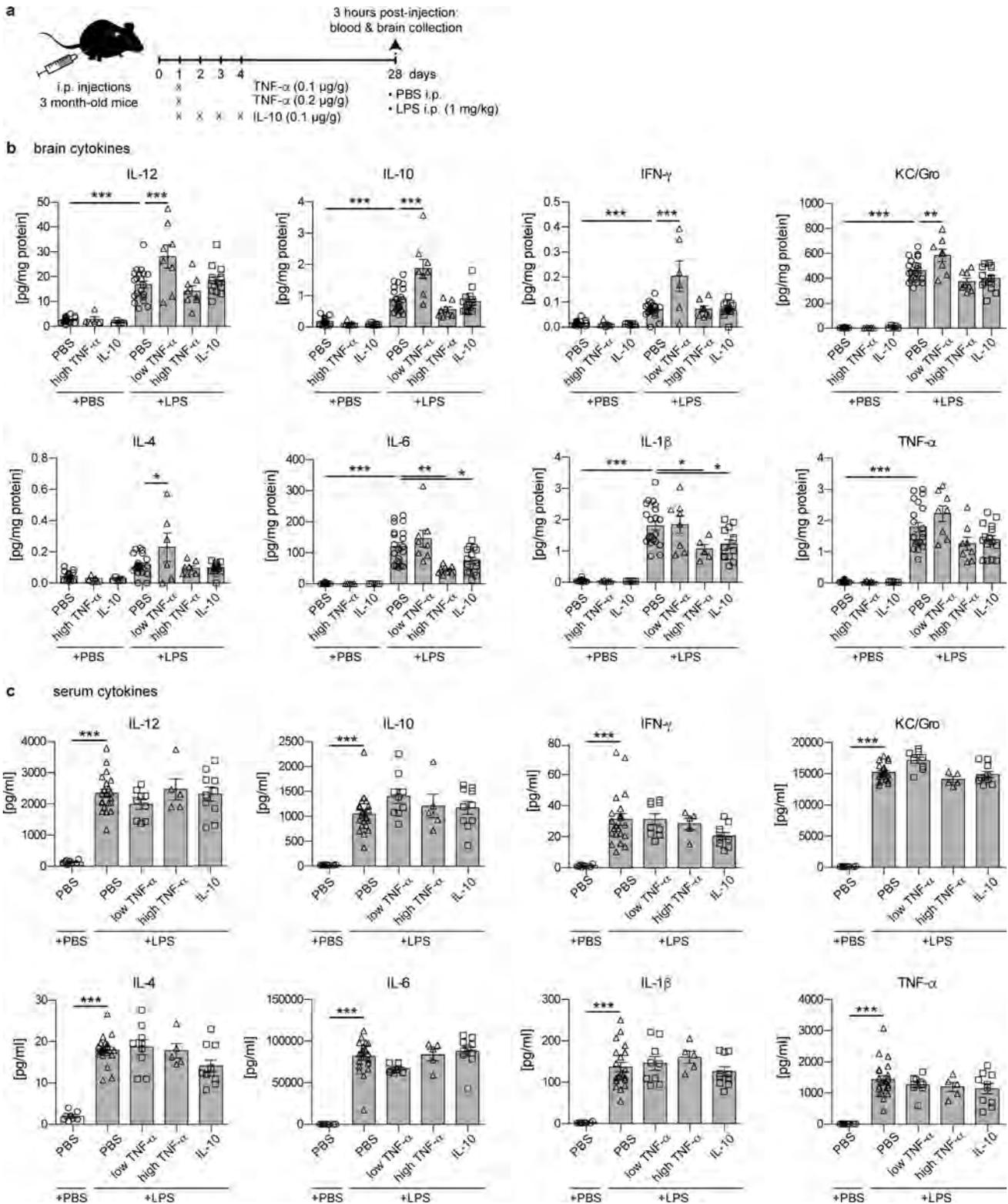
**Extended Data Fig. 9 | Peripherally applied cytokines induce immune memory in the brain. a**, Experimental design. **b**, Cytokine responses in the brain, four weeks after peripheral cytokine application ($n = 17, 5, 5, 21, 8, 8, 15$ mice from left to right). Note that TNF dose-dependently enhances (low dose) or decreases (high dose) certain cytokines. Similar to high dose TNF, certain cytokines are also reduced by peripheral application of IL-10 four weeks earlier. **c**, Cytokine responses in the periphery are unaffected ($n = 8, 21, 9, 5, 10$ mice). Data are means ± s.e.m. $*P < 0.05$, $**P < 0.01$, $***P < 0.001$ for one-way ANOVA with Tukey correction.